

Drew University
College of Liberal Arts

Methods for Characterizing a Confocal Microscope with Optical Phantoms

A Thesis in Physics
by
Zoe Hughes

Submitted in Partial Fulfillment
of the Requirements
for the Degree of
Bachelor in Arts and Baldwin Honors Program
With Specialized Honors in Physics

May 2017

Abstract

Confocal microscopes can produce high-resolution images of thick biological samples. Before biological samples can be imaged, a microscope needs to be characterized and calibrated with optical phantoms, which are artificial specimens that mimic the optical properties of biological samples. I designed and built a custom reflectance scanning confocal microscope that operates at a wavelength 660 nm. I assessed the confocal microscope's axial sectioning with two sets of optical phantoms. With the optical phantoms, I aimed to mimic human skin that has a scattering coefficient in the range 30 to 70 cm^{-1} . The optical phantoms were a mixture of Polydimethylsiloxane (PDMS), a plastic-like material, and a scattering material Min-U-Sil40. I developed an apparatus and method for measuring the scattering coefficient of the optical phantoms. The first set consisted of four samples with the same scattering coefficient, 2 cm^{-1} , but different thicknesses. The second set consisted of three samples: two with the same scattering coefficient, around 118 cm^{-1} , and one with a scattering coefficient of 35 cm^{-1} . All three samples varied in thickness. With the low scattering coefficient, I found that variations in the optical phantom's thickness had no effect on the axial sectioning. With the high scattering coefficient, I concluded that the axial sectioning was affected by changes in thickness. The optical phantom mixture proved to be a success because it was capable of mimicking human skin and tissue. It was also stable and could be reused multiple times. Further research is needed to prepare the microscope to image live biological samples.

Acknowledgements

I would like to thank Dr. Bjorg Larson for giving me such great guidance throughout this entire project. Thank you for giving me this opportunity to work with you. You are an amazing mentor and have taught me not only physics, but lessons I will use beyond Drew. Thank you to my thesis committee members, Dr. Roger Knowles and Dr. Jim Supplee, for giving me their time and insightful guidance. It was really a pleasure to work with you. Thank you to Kelsey Oeler for being my lab partner. I enjoyed research so much more when you were there. Thank you for listening to all my troubles when the microscope was misbehaving. Only you truly understood the struggle! Thank you endlessly to Danielle Dorvil and Drexel Formoso for reading this paper and listening to me perform my presentation over and over again, all while keeping a smile on your faces the whole time. You both made sure I was actually making any sense. Finally, thank you to my parents for their never ending support and love. Without the values you have instilled in me, I could never have accomplished this.

Table of Contents

1. Introduction	1
1.1 Interest in Confocal Microscopy	1
1.2 Confocal Microscopy.....	3
1.2.1 History of Confocal Microscopy.....	7
1.2.2 Fluorescence Confocal Microscopy	8
1.2.3 Reflectance Scanning Confocal Microscopy.....	11
1.2.4 Other Scanning Methods	12
1.3 Applications	14
1.3.1 Biological	14
1.3.2 Clinical	15
2. Theory	16
2.1 Light and How It Propagates.....	16
2.1.1 Optical Properties	17
2.1.2 Refraction	19
2.1.3 Reflection.....	20
2.2 Axial Sectioning and Pinhole Size	21
2.3 The Scattering of Light and the Scattering Coefficient.....	25
2.3.1 Beer-Lambert Law.....	25
2.3.2 Optical Phantoms	27
3. Building the Confocal Microscope.....	29
3.1 Equipment Used.....	29
3.2 Methods	33
3.2.1 Setup I	34
3.2.2 Setup II.....	36
Axial Sectioning: Air Lens	37
Axial Sectioning: Oil Lens.....	40
Optical Phantoms: Milk and Water Mixture	42
Characterization of the Microscope	46
3.2.3 Setup III.....	49
4. Data and Analysis	53
4.1 Set One: Low Effective Scattering Coefficient.....	54
4.1.1 Determining Effective Scattering Coefficient.....	54
4.1.2 Axial Sectioning Results and Analysis.....	56
4.2 Set Two: High Effective Scattering Coefficient.....	61
4.2.1 Determining Effective Scattering Coefficients.....	61
4.2.2 Measuring Thickness.....	62
4.2.3 Axial Sectioning Results and Analysis.....	64
4.3 Future Steps and Techniques	71
4.4 Pilot Study.....	73
5. Conclusion.....	77
References	79

List of Figures and Tables

Figure 1: Widefield vs. Point Scanning.....	1
Figure 2: The Concept of Confocal Microscopy.	4
Figure 3: Airy Disc.....	4
Figure 4: Diffraction Pattern.	5
Figure 5: Lateral and Axial Resolution..	6
Figure 6: Axial Sectioning Data Collection..	7
Figure 7: Basic setup of a fluorescence confocal microscope.....	9
Figure 8: Basic setup of a reflectance scanning confocal microscope.	11
Figure 9: Electromagnetic Wave..	17
Figure 10: Snell's Law and the Law of Reflection.....	19
Figure 11: Axial Sectioning vs. Pinhole.....	23
Figure 12: Beer-Lambert Law.....	26
Figure 13: Setup I.....	35
Figure 14: Setup II.....	36
Table 1: Results of FWHM Calculations for Pinholes 100, 150, and 200 μm Using Air Lens.....	38
Figure 15: Averaged Axial Sectioning Graphs for Pinholes 100, 150, and 200 μm..	40
Table 2: Theoretical FWHM vs. Experimental FWHM for 100, 150, 200 μm Pinholes	40
Figure 16: Bridge Method for Water Sample Mounting With Oil Lens..	41
Table 3: Results of FWHM Calculations for Pinholes 100, 150, and 200 μm Using Oil Lens.....	41
Figure 17: Axial Sectioning Graph for 100 μm Pinhole With Water Sample.....	42
Figure 18: Scattering Coefficient Apparatus	44
Figure 19: Bridge Method for Mounting Optical Phantom Samples With Oil Lens.	
Table 4: Effective Scattering Coefficient Measurements for 50%, 66%, and 83% diluted solution optical phantoms..	45
Figure 20: $\ln(I/I_0)$ vs. z for 50%, 66%, and 83% Diluted Solutions.	46
Figure 21: (a) Axial Sectioning Data of Water Compared with 10% Diluted Solution. (b) Axial Sectioning Data of Water Compared with 30% Diluted Solution. (c) Axial Sectioning Data of Water Compared with 50% Diluted Solution. All of the graphs are the average of five trials.	48
Table 5: Comparison of FWHM of Axial Sectioning of Water vs. Optical Phantoms.	49
Figure 22: Setup III.	50
Table 6: Results of FWHM Calculations for Pinholes 15, 30, 40, 50, and 100 μm Using Air Lens.....	51
Figure 23: Axial Sectioning Data for 15, 30, 40, 50, and 100 μm Pinholes.	52
Table 7: Theoretical FWHM vs. Experimental FWHM for 15, 30, 40, 50, 100 μm Pinholes	53
Table 8: Effective Scattering Coefficient Measurements for Samples with Thicknesses: 200, 260, 280, and 380 μm.....	55
Figure 24: Intensity Relationship with Thickness for Samples 200, 260, 280, and 380 μm Thick.....	55

Figure 25: Three Reflections Axial Sectioning Graphs.	56
Figure 26: Axial Sectioning Data Graphs for the PDMS, Glass and Paper at the Focal Plane.	57
Figure 27: Axial Sectioning Data Graphs for Air, and Samples 200, 260, 280, and 380 μm.	59
Figure 28: Axial Response Graph.	60
Table 9: Effective Scattering Coefficient Data for Samples A, B, and C.	62
Table 10: Range of μ's (cm^{-1}) for Samples A, B, and C. Each sample had a range of μ's because of the surface variation.	62
Figure 29: Thickness and Spin Rate.	64
Table 11: Axial Sectioning Data for Samples A, B, C with 50 μm Pinhole.	65
Figure 30: Axial Sectioning Comparison Graphs for Samples A, B, and C with 50μm pinhole.	67
Figure 31: Stony Brook Comparison Axial Response.	68
Table 12: Comparison of Stony Brook Data to My Data.	69
Table 13: Axial Sectioning Data for Samples A, B, C with 100μm Pinhole.	74
Figure 32: Axial Sectioning Comparison Graphs for Samples A, B, and C With the 100 μm pinhole.	76

1. Introduction

1.1 Interest in Confocal Microscopy

Confocal microscopes offer multiple features that exceed the abilities of conventional widefield microscopes. With widefield microscopes, samples need to be sliced into thin sections in order to be examined. Only the top surface of the sample can be viewed. However with confocal microscopes, thick samples can be inspected through deep optical sectioning, a noninvasive method that uses focused light to section the sample, instead of physically altering it [1]. Through point scanning, which builds an image using a point beam, three-dimensional images of the sample can be compiled. Widefield scanning and point scanning are compared in Figure 1.

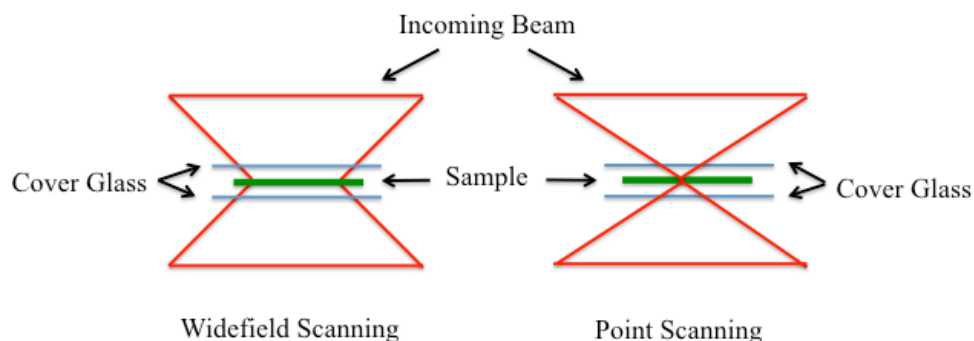


Figure 1: Widefield vs. Point Scanning. With widefield scanning, the sample needs to be thin. Light is focused to a plane, which is fixed. The whole sample is illuminated and the image is collected at once. With point scanning, the sample can be thicker. Light is focused to a point, which can move within the sample. The image is built point-by-point and assembled by a computer.

Widefield scanning requires a thin sample because focused as well as out-of-focused light is used to form the image; the focal plane is fixed. Point scanning illuminates the sample a single spot at a time. Only focused light collects the image. Optical sectioning is possible because the focal plane can move horizontally and vertically through the sample, so sections that were originally unreachable can be clearly imaged [2].

A defining feature of a confocal microscope is a pinhole that is positioned in front of the detector. Blurry images caused by reflections and fluorescent light scattering is a common problem when using widefield microscopes. With a confocal microscope, this problem is averted because the pinhole excludes all out-of-focus light [3]. Because of this defining feature, this microscope can produce vivid images in higher resolution than images collected using a widefield microscope.

Because of these unique advantages, deep optical sectioning and high resolution, confocal microscopes have been incorporated into biological research and clinical uses. Deep optical sectioning has improved the way scientists examine specimens because sample observations can be carried out in a noninvasive way. Accordingly, there has been encouragement to increase the use of these microscopes and develop new types to satisfy the various needs of researchers. Biological research focuses on investigating specimens, such as human cell lines and tissue and as this research has matured, more clinical uses have been developed such as diagnosing skin abnormalities in patients. I am particularly interested in this clinical application, especially point-of-care pathology. Confocal microscopy allows researchers to quickly diagnose cancer in patients in a single visit through deep optical sectioning of skin. This technique simplifies the process of diagnosis and enables a more efficient practice of patient care. A specific microscope that has shown incredible potential in point-of-care pathology is the reflectance scanning confocal microscope.

In order to design more effective optics for biological samples, I have constructed a reflectance scanning confocal system. However before I am able to image live samples, the microscope needs to be evaluated on its axial sectioning. The purpose of this study is

to build a confocal microscope and develop a method for assessing this system by imaging optical phantoms, which mimic the scattering properties of actual specimens. I aim to determine a relationship of how the axial sectioning is affected by variations in the optical phantoms' thickness and scattering coefficient. Other objectives are to measure how accurate the system is in comparison with the standardized results from previous studies and strategize the following steps needed to prepare the microscope to image biological samples. The ultimate goal of my research is to develop a method to characterize confocal microscopes, which will enhance the use of them in clinical applications and thus improve lives of patients.

1.2 Confocal Microscopy

Confocal microscopes are commonly used in studying biological samples because they are capable of optical sectioning and high resolution. These abilities are possible because of the pinhole in the system [2]. The concept of confocal microscopy is shown in Figure 2 below.

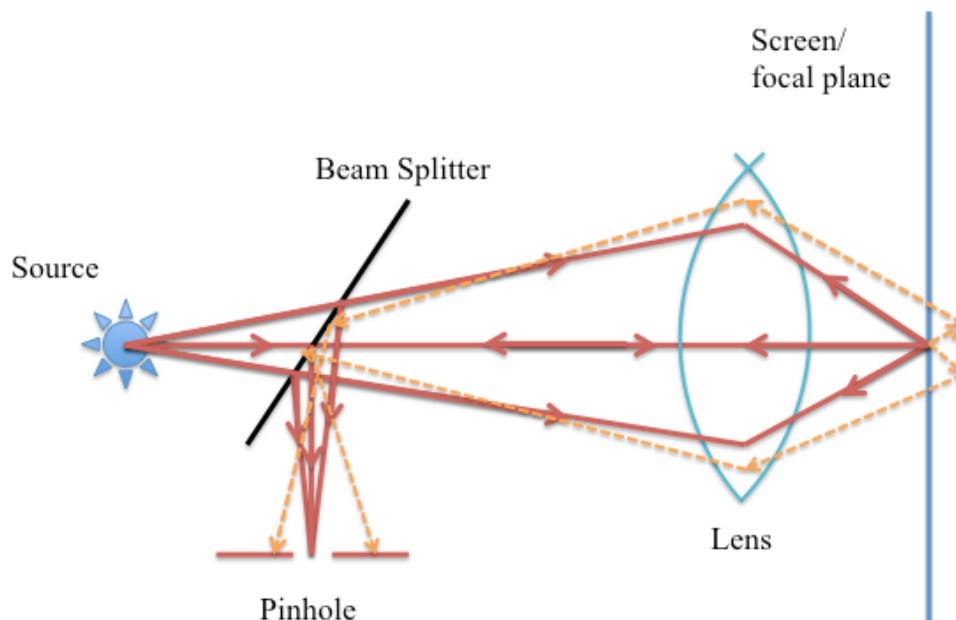


Figure 2: The Concept of Confocal Microscopy. Light that is focused before or after the screen does not refocus at the pinhole and therefore cannot reach the detector that is behind the pinhole. The pinhole blocks unfocused light because only the light focused at the focal plane can travel through. With a computer, detailed three-dimensional models can be digitally compiled from all the images of the sample.

Only light focused in the focal plane can travel through the pinhole and reach the detector. When light passes through the pinhole, a diffraction pattern, a bright disk with concentric rings of alternating maximum and minimum intensities, is produced. The central bright disc of the pattern is called the Airy disc. The angular radius of the Airy disc depends on the wavelength of the light and diameter of the pinhole [4]. The diffraction pattern for a pinhole is displayed in Figure 3.

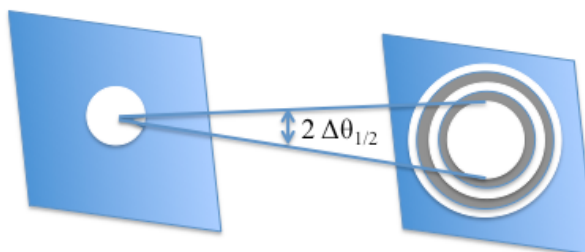


Figure 3: Airy Disc. When light travels through a circular aperture, or pinhole, a diffraction pattern is the result. From the left, light shines through a pinhole and a diffraction pattern is produced on a screen on the right. The pattern consists of intensity maximums and minimums due to constructive interference, the addition of light waves, and destructive interference, the cancelation of light waves. In the center, the light

experiences constructive interference and produces the central maximum, called the Airy disc. The angular radius, $\Delta\theta_{1/2}$, of the disc depends on the wavelength of the light and the size of the pinhole.

The resolution of the microscope is limited by the diffraction because the image of the sample will lie within the central disc [4]. Resolution also relies heavily on the pinhole size, which is discussed in detail later in Section 2.2. Resolution occurs when two point sources at minimum distance can still be distinguished separately [2]. Two images are resolved when their Airy discs are separated. For two images to be resolved, their minimum separation distance, x_{min} , is determined by the equation:

$$x_{min} = f \left(\frac{1.22\lambda}{D} \right) \quad (1),$$

where f is the focal length of the objective lens, D is the diameter of the objective lens, and λ is the wavelength of the light. The ratio D/f is the numerical aperture [4]. The numerical aperture describes the objective lens' ability, and so essentially the microscope's ability, to collect light and resolve the specimen [5]. The numerical aperture plays an important role in axial resolution, which is addressed further in Section 2.2.

Figure 4 shows examples of two resolved and unresolved point sources.



Figure 4: Diffraction Pattern (a) Two resolved point sources. The Airy discs are separated by at least the minimum distance needed for the image to be resolved. (b) Two unresolved point sources. The Airy discs overlap and do not meet the minimum separation distance to be resolved.

Types of resolution include lateral resolution and axial resolution, as illustrated in Figure 5.

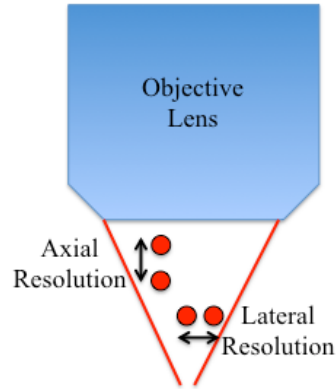


Figure 5: Lateral and Axial Resolution. Lateral resolution is measured parallel to the focal plane. Axial resolution is measured perpendicular to the focal plane and parallel to the beam of light. [4]. With thick samples, high axial resolution is required to distinguish between the different layers.

In this study, I am focusing on the axial resolution of the confocal system because high resolution in the axial direction is needed for axial sectioning, or imaging through the layers of a thick sample. Axial sectioning data is collected when the sample moves through the focal plane. Figure 6(a) illustrates this process and Figure 6(b) shows an example of a typical axial sectioning graph, a Gaussian curve. As the sample moves through the focal plane, the detector signal changes. The maximum amount of light through the detector occurs when the sample is at the focal plane. The least amount of light through the detector occurs at the beginning and end of the sample's travel because the out-of-focused light is blocked by the pinhole. Axial sectioning is defined by the full width half max (FWHM), the width of the curve at half of the maximum. This value is determined by the size of the pinhole. The theory and calculations that define the relationship between pinhole size and FWHM are discussed further in Section 2.2.

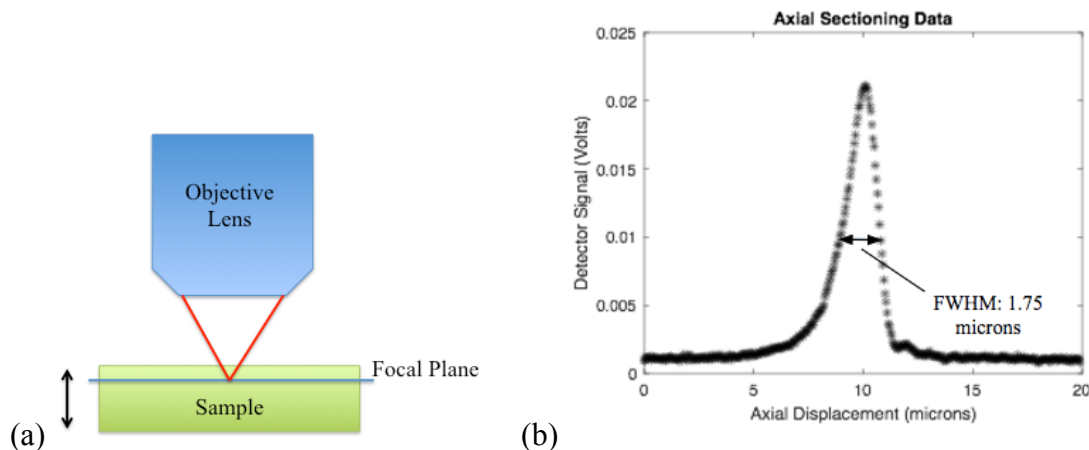


Figure 6: (a) Axial Sectioning Data Collection. Axial data is collected as the sample is moved through the focal plane. The amount of light able to reach the detector behind the pinhole is maximum when the sample is at the focal plane. (b) Graph of Axial Sectioning Data. The relationship between the detector signal and the axial displacement of the sample is a Gaussian curve.

1.2.1 History of Confocal Microscopy

Confocal microscopy originates from the development of light microscopy. The study of light microscopy provides important insights into improving and understanding lateral resolution, axial resolution, and depth of field of a microscope. In 1873, Ernst Abbe investigated these three fundamental ideas. Optimal lateral resolution occurs when two point sources at minimum distance can still be distinguished separately. These points are measured along the focal plane. Similarly, optimal axial resolution is achieved when two points perpendicular to the focal plane and parallel to the beam of light are separately distinguished. Depth of field of a microscope determines the depth of the image. The depth of field can often be obstructed by out-of-focus light, which makes it hard to measure [2]. These three aspects founded in light microscopy provide the grounds for confocal microscopy.

Marvin Minsky, a scientist at Harvard University, patented the first confocal microscope in 1957. His microscope used a stage-scanning optical system. Minsky was interested in observing living cells and tissues. He aimed to image neural activity of a living brain. Minsky's microscope had two pinholes [2]. The pinholes reduced the blurring of images by blocking the scattered light, a revolutionary concept no one had thought of before. This microscope allowed wider scans of the x and y axes and even included the z-axis. It also had improved resolution and could produce clear images of thick specimens. Previous microscopes could only give a narrow view of a thinly sliced specimen and the z-axis was not adjustable [2].

In the early 1970s, M. David Egger and his colleagues at Yale University created a laser-illuminated confocal microscope, known today as the confocal laser-scanning microscope. In this kind of microscope, the objective lens oscillates so the laser scans over the specimen. In 1972, Egger got a patent for the invention. In Europe in the late 1970s and early 1980s, scientists started using confocal imaging for cellular biology. Finally in 1987, the confocal microscope was put on the market for purchase [2]. Variations of confocal microscopes have been developed through the years, but the two general types are fluorescence and reflectance scanning.

1.2.2 Fluorescence Confocal Microscopy

In fluorescence confocal microscopy, the specimen is coated with a fluorescent dye or fluorophores. The incoming beam or excitation light stimulates the fluorophores on the sample. The fluorophores absorb the incoming light and its electron becomes excited. The excitation may last from one to ten nanoseconds and then the electron falls to a lower more stable energy level. Energy is released as fluorescence and the electron

falls back to its resting state [6]. The wavelength of the light emitted is longer than the wavelength of the excitation light because there is a decrease in energy. The difference between the excitation maximum wavelength and the emission maximum wavelength is called the Stokes shift [7].

The fluorophores allow specific parts of a specimen to be distinguishable [8]. For instance, the dye can tag different proteins and molecules of interest in skin and tissue samples. The basic setup for a fluorescence confocal microscope is shown in Figure 7.

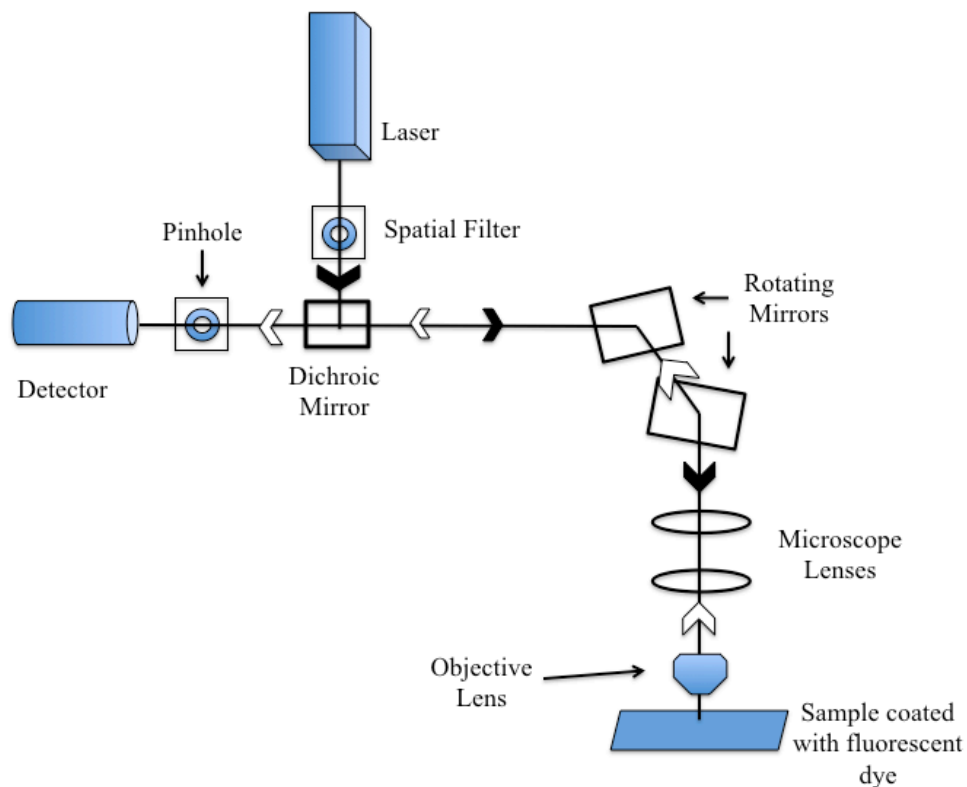


Figure 7: Basic setup of a fluorescence confocal microscope. The black arrows represent the incoming beam path. The white arrows represent the returning beam path. The rotating mirrors scan both the incoming and returning beams. The dichroic mirror reflects the incoming beam and transmits the returning beam. The detector is connected to a computer (not shown) that constructs the image pixel by pixel.

A laser provides the excitation light to reduce the time it takes to build an image.

Each point of the sample must be illuminated long enough so an adequate amount of light is gathered. The laser first goes through a spatial filter. The spatial filter is placed in the

system to shape the beam, so only the central maximum of the laser can pass through [9]. A dichroic mirror reflects the incoming beam to the rotating mirrors. The dichroic mirror controls the wavelengths that pass through by reflecting light of certain wavelengths and transmitting others. The two scanning mirrors direct the beam across the specimen. Light of a different wavelength is emitted from the specimen and reflected back through the rotating mirrors. Light is transmitted through the dichroic mirror and travels through the pinhole that is lined up with a detector [6]. The pinhole is different from the spatial filter because it performs the crucial jobs of blocking the out-of-focus light from the detector and determining the microscope's axial resolution. A computer is connected to the detector that processes each pixel into an image [1]. The time to build the entire image may range from less than a second to a few minutes and depends not only on the intensity of the light source, but also on the speed of the rotating mirrors.

When using this microscope, the type of fluorophore used needs to be chosen with care. Depending on the portion that is coated and type of specimen, the appropriate fluorophore and concentration is required. Considerations must be taken with living specimens because they might be damaged by the fluorophores. Another challenge with fluorophores is photo bleaching, which occurs when the dye fades due to overexposure of excitation light. Some preventative measures to reduce photo bleaching are lowering the magnification so the excitation light spreads out and displaying the sample in another gas other than oxygen, which advances photo bleaching [8]. Taking into account these concerns, the fluorescence confocal microscope has many beneficial biological applications, which are further discussed in the Applications section, 1.3. The other type

of microscope, the reflectance scanning, has a lot in common with the fluorescence confocal microscope.

1.2.3 Reflectance Scanning Confocal Microscopy

The reflectance scanning confocal microscope has a setup similar to the fluorescence confocal microscope, however fluorophores are not used on the specimen. The wavelength of the laser beam remains constant throughout the system. Instead of using a dichroic mirror that transmits the returning beam, a polarizing beam splitter is used. A polarizing beam splitter is not dependent on wavelength, like the dichroic mirror, but rather depends on the polarization of light [4]. Figure 8 shows the basic setup for the reflectance scanning confocal microscope.

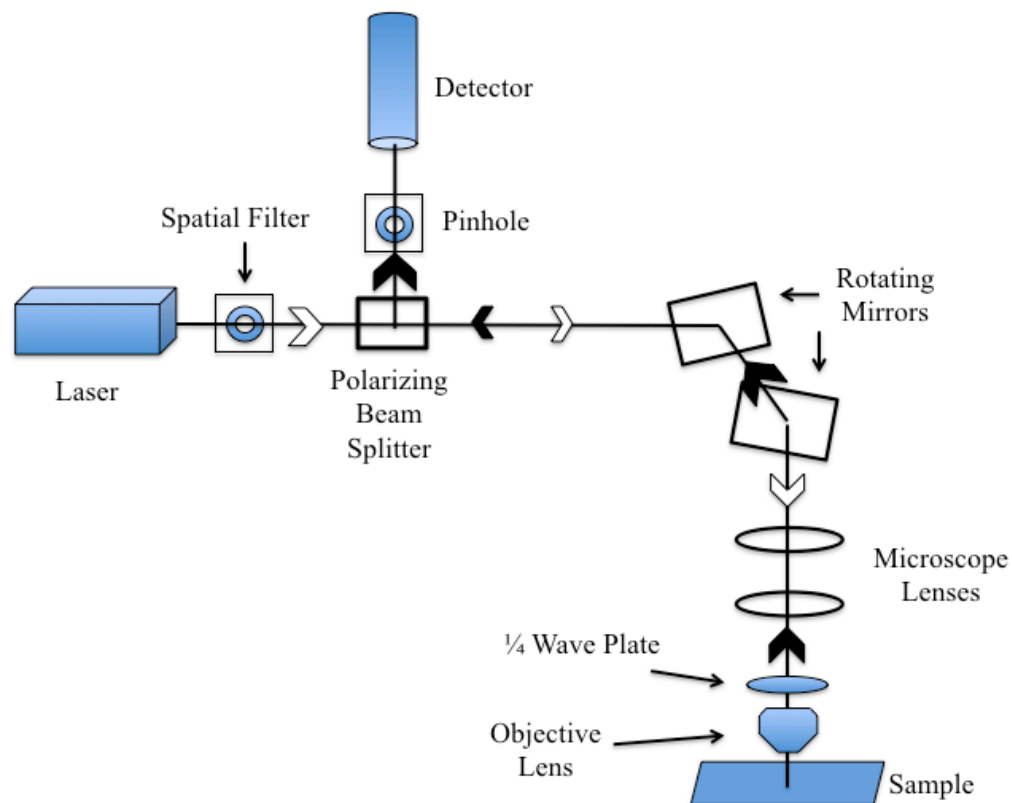


Figure 8: Basic setup of a reflectance scanning confocal microscope. The white arrows represent the incoming beam and the black arrows represent the returning beam. Both beams are the same wavelength. The polarizing beam splitter separates the beam due to the polarization. The incoming beam is not permitted to travel to the detector; it is

transmitted through to the rotating mirrors. The $\frac{1}{4}$ wave plate changes the polarization of the beam. The returning beam is reflected to the detector, which is connected to a computer (not shown) that constructs the image.

A laser supplies the light source for this microscope. At the start, the light is vertically polarized and first travels through the spatial filter. The light is transmitted through the polarizing beam splitter and is directed with the rotating mirrors towards the sample. The $\frac{1}{4}$ wave plate changes the vertical polarization to circular polarization. The beam scans the sample and reflects back. This time the $\frac{1}{4}$ wave plate converts the light to horizontal polarization, so now the polarizing beam splitter reflects the light towards the detector [6]. With reflectance scanning, the sample is analyzed through three-dimensional imaging.

As with any system, limitations of this microscope exist. The image construction process may take time because the detector can only read one pixel at a time and the rotating scanning mirrors are only able to go so fast. Alignment is also an important factor in confocal microscopes because light has to travel from the lens and pass through the pinholes in order for an image to appear in focus. This is why the microscope's objective lens must be accurate. A well-corrected objective lens must have any aberrations, both lateral and longitudinal, corrected and be able to transmit light over the needed wavelength range. Lastly, confocal microscopes are prone to vibrational and mechanical problems [2]. The next section addresses other possible scanning methods.

1.2.4 Other Scanning Methods

Besides point scanning, other scanning techniques include line scanning, stage scanning, and the tandem scanning with the Nipkow Disk [10]. Similar to how point scanning uses a focused beam to scan the sample, line scanning uses a focused line or slit

of light. The construction of the image is faster with line scanning than point scanning because only one-dimensional scans are necessary. However, the challenge with line scanning is background noise. The out-of-focus light is not blocked along the illumination slit and this produces poor resolution and FWHM sectioning [10]. One study done at Blakett Laboratory at the Imperial College London was conducted to develop techniques to reduce this out-of-focus light. The scientists were successful in this mission by using an array detector instead of a line detector and saw great improvement in resolution. For more details on this study see Reference [10].

Stage scanning was the method Minsky, the inventor of the confocal microscope, originally used. The stage scanning confocal microscope is able to block out most of the excess light. Using a tuning fork device, the stage moves to scan the specimen, instead of the laser beam; yet, the downside to this method is the length of time it takes. Compared to the scanning mirrors, the scanning stage simply cannot move as fast [11]. The speed of the scanning, whether with the stage or the mirrors, determines the pixel rate or how fast a pixel of the image can be produced with the computer. This in turn determines the frame rate, or the rate at which the image is produced. A typical size of a frame might be 500 x 500 pixels [2]. Stage scanning yields great resolution and is a good method if time is not a pressing concern.

Lastly, a fast scanning option is tandem scanning with the Nipkow disk. This type of microscope uses multiple pinholes and the light travels through all of them simultaneously [2]. Numerous points of the sample are illuminated at once, so images can be created at a faster rate, yet the amount of light that makes it back through the pinholes

is minimal. With a low detector signal, problems can arise because a strong signal is needed for high image quality [8].

For the purposes of my research, tandem scanning would not be the ideal scanning method because image quality and resolution is the main focus. Furthermore, this project is also time sensitive, so the stage scanning method would be too time consuming. Line scanning would have been possible, but I chose point scanning because it offers higher resolution.

1.3 Applications

1.3.1 Biological

When imaging living cells, tissue, and other biological specimens, scientists often use confocal microscopes because they are able to examine thick samples without physically cutting into them. Fluorescence confocal microscopes are commonly used in biological research because fluorescence dyes can highlight portions of the specimen. For instance, specific molecules may be labeled with color dyes to distinguish different characteristics of cells [8]. In one study, researchers labeled brain tissue from Alzheimer's disease patients in order to determine the spatial relationship between the pathologies of plaques and tangles [43]. Because the pinhole rejects out-of-focus light, the images of a confocal microscope are clearer than images from a widefield microscope.

Various types of confocal microscopes are used in biology. The most common types use the beam to scan the sample. There is single beam and multiple beam scanning. Point scanning with a single beam is the most popular technique. Tandem-scanning with

the Nipkow disk can use multiple beams in the system. This microscope is able to detect low fluorescent levels and collect the image quickly [1]. Because they have the ability to construct detailed three-dimensional structures from two-dimensional images, confocal microscopes are the optimal choice for biological research [8].

1.3.2 Clinical

Confocal microscopes are also employed in clinical uses focused on diagnosing cancer. The traditional procedure for diagnosing cancer without a confocal microscope usually takes up to a couple days. A biopsy of the skin needs to be taken. The sample is then frozen, so it can be sliced into thin sections. The sample also needs to be stained for contrast, so scientists can identify its elements. After these steps, scientists can examine the sample under a microscope and make a diagnosis [11]. With confocal microscopes, instead of a skin biopsy, the patient can be examined under the microscope and scientists are able to extract information about their cells in a noninvasive way. The confocal microscopes can section deep within the skin and generate clear images. For instance, in some clinical studies the diagnosis of melanoma and ovarian cancer can be given *in vivo*, or in a living human [12]. Both reflectance and fluorescence imaging are utilized in clinical use. With fluorescence confocal microscopes, the drawback is dye has to be used, but with reflectance scanning confocal microscopes no dyes are needed. Scientists can examine skin lesions with optical sectioning and diagnose cancers like melanoma. The cellular detail is revealed with reflectance imaging and any abnormalities are identified. Ophthalmology, the study of eye diseases, also uses this type of microscope [12].

There has recently been encouragement from researchers to increase the number of confocal microscopes in clinical use [2]. This has led to the development of new

microscopes and comprehensive studies on their specific characteristics. As stated before, the motivation for my research is to develop a method to characterize the axial sectioning of a custom made reflectance scanning confocal system. Yet before discussing the specifics on how the microscope was developed and the methods used for assessing it, the theory of light and how it behaves in a medium, as well as the theory of a confocal microscope's resolution must first be addressed.

2. Theory

2.1 Light and How It Propagates

Light is made up of oscillating electric and magnetic fields. Figure 9 illustrates light, also known as electromagnetic waves. Observe in the figure that the electric and magnetic fields oscillate perpendicular to each other and perpendicular to the propagation of the wave. The direction the wave oscillates determines its polarization [13]. The distance from one peak to the next peak is the wavelength of the wave. The wavelength of light can range from around 3×10^{-15} meters (m), the length of gamma rays, to approximately 300 m, the length of radio waves. The wavelength determines the color of the light [13]. The way light interacts with different media, such as human skin, depends on the wavelength and the optical properties of the medium. By examining the optical properties and the process of refraction and reflection, an understanding of how the light interacts with the sample can be achieved.

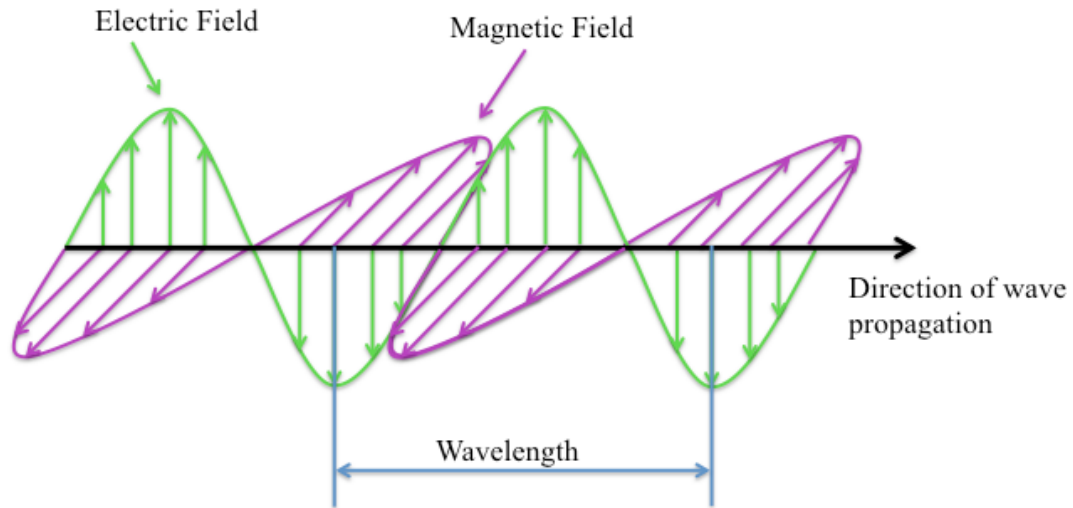


Figure 9: Electromagnetic Wave. The electromagnetic wave is composed of electric and magnetic fields and it propagates perpendicular to both fields. This image is typically associated with the structure of plane waves [13].

2.1.1 Optical Properties

When light encounters a new material, the propagation of the wave changes. This change is attributed mainly to three optical properties: refractive index N , absorption coefficient μ_a , and scattering coefficient μ_s . It is crucial to be informed about these optical properties when examining biological specimens because they affect the contrast and resolution of the image [14].

To begin with, the index of refraction is an optical constant that indicates how light will travel through a given material. The index of refraction, N , is complex,

$$N = n + ik \quad (2).$$

The real component, n , is inversely proportional to the phase velocity, or the velocity at which the crests of the waves propagate. The equation

$$n = \frac{c}{v} \quad (3),$$

illustrates this, where n is the real index of refraction, v is the speed of the wave, and c is the speed of light. The imaginary component, k , describes the loss of the light wave due

to absorption. A material can speed up or slow down a wave. For instance, if the light wave travels from a lower index of refraction to a higher one, then the speed decreases. On the other hand, if the wave travels from a higher index of refraction to a lower one, then the speed increases [13]. Besides the speed of the wave, the intensity is also affected.

Sometimes light is lost when it enters a new medium; this loss can be quantified in intensity, I , by observing the brightness before and after the material. Intensity describes the average power transferred over an area and has the units $watts/meter^2$ [4]. The intensity is proportional to the square of electric field: $I \propto |E|^2$ [13]. The loss of light described by the imaginary part of the refractive index, k , is due to only absorption. The absorption coefficient, μ_a , is an optical constant that indicates how absorptive a material for a specific wavelength is. A high value for μ_a signifies the material is greatly absorbent. A low value for μ_a is around 10 cm^{-1} , while a high value is 10^6 cm^{-1} [13]. Besides absorption, light may also be lost due to scattering. Similar to the absorption coefficient, a high scattering coefficient, μ_s , indicates a material scatters a large amount of light. A typical value for μ_s might range from 100 cm^{-1} to 400 cm^{-1} [14]. The loss of light due to both scattering and absorption is described by the attenuation coefficient, μ , where

$$\mu = \mu_a + \mu_s \quad (4).$$

The attenuation coefficient indicates the turbidity level or cloudiness, specifically the loss of intensity per unit length, through the medium [15].

Light can refract and reflect when it hits a new material. These three optical constants, N , μ_a , and μ_s , determine the propagation of a wave through a medium. For

instance, both refraction and reflection are dependent on the index of refraction and the angle of the incoming light. The absorption and scattering coefficients influence the refracted light's travel and the amount of light that can reflect back out of the material. Hence, the refraction and reflection of light are determined by these optical properties of a material.

2.1.2 Refraction

The refraction of light follows Snell's law [13]:

$$n_1 \sin \theta_i = n_2 \sin \theta_t \quad (5).$$

Snell's law makes use of only the real part of the index of refraction. Figure 10 shows the paths of refraction and reflection of light when incident on a new medium.

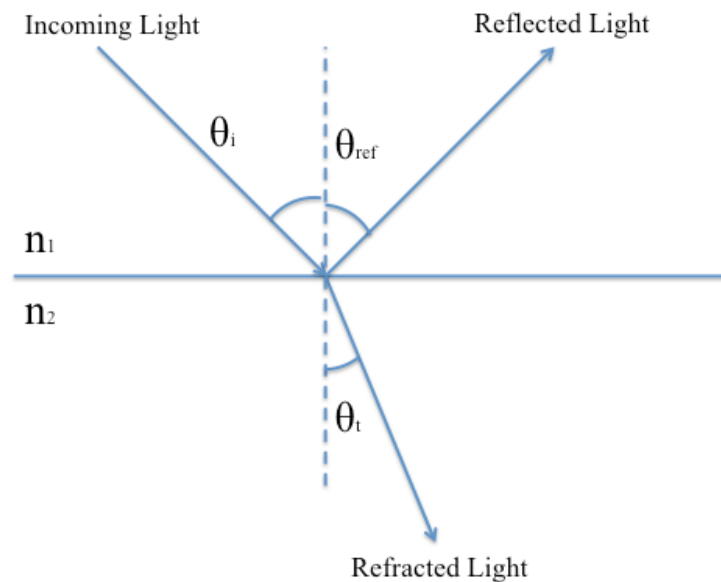


Figure 10: Snell's Law and the Law of Reflection. When light is incident on a new surface, it may refract and reflect. The refracted light obeys Snell's Law and the reflected light obeys the Law of Reflection, which says the angle of incidence is equal to the angle of reflection.

Note that in Figure 10, the light is traveling from a smaller to larger index of refraction because the refracted light bends towards the normal. If the light went from a larger to smaller index then the light would bend away from the normal. Not all of the light

refracts through the material. Some of the light does not enter the medium at all and instead reflects off of it.

2.1.3 Reflection

The reflection of light follows the Law of Reflection:

$$\theta_i = \theta_{ref} \quad (6).$$

As seen in Figure 10, the angle of incoming light measured relative to the normal is equal to the angle of the reflected light, also relative to the normal. The amount of light that is transmitted and reflected through a material is based on the Fresnel coefficients:

$$r_s = \frac{E_r(s)}{E_i(s)} = \frac{n_i \cos \theta_i - n_t \cos \theta_t}{n_i \cos \theta_i + n_t \cos \theta_t} \quad (7)$$

$$t_s = \frac{E_t(s)}{E_i(s)} = \frac{2n_i \cos \theta_i}{n_i \cos \theta_i + n_t \cos \theta_t} \quad (8)$$

$$r_p = \frac{E_r(p)}{E_i(p)} = \frac{n_i \cos \theta_i - n_t \cos \theta_t}{n_i \cos \theta_i + n_t \cos \theta_t} \quad (9)$$

$$t_p = \frac{E_t(p)}{E_i(p)} = \frac{2n_i \cos \theta_i}{n_i \cos \theta_i + n_t \cos \theta_t} \quad (10).$$

The Fresnel coefficients indicate how much of the incident light is transmitted or reflected. Reflectance, r , is the ratio of the reflected amplitude of the electric field to the incident amplitude of the electric field. Transmittance, t , is the ratio of the transmitted to the incident amplitude of the electric field. The subscripts s and p denote the polarization: s represents the perpendicular polarization and the p represents the parallel polarization to plane of incidence [13]. The reflection and transmission of light are dependent on the index of refraction and the angle measured from the normal. Furthermore, now that the theory of how light behaves and interacts in different mediums has been established, the theory of resolution in a confocal system must be discussed.

2.2 Axial Sectioning and Pinhole Size

The size of the pinhole in a confocal imaging system is crucial to get optimal resolution and optical sectioning. As mentioned previously, axial sectioning is defined by the FWHM. The FWHM of the curve depends on the size of the pinhole. Confocal systems require different pinhole sizes for the best results. By using a theory developed by T. Wilson and A.R. Carlini, a prediction for the FWHM can be made and an ideal pinhole size for a particular system can be calculated [16]. In their paper, Wilson and Carlini show that the intensity of the signal at the detector is a function of the normalized optical units v , and u , which are dependent on real radial and axial coordinates:

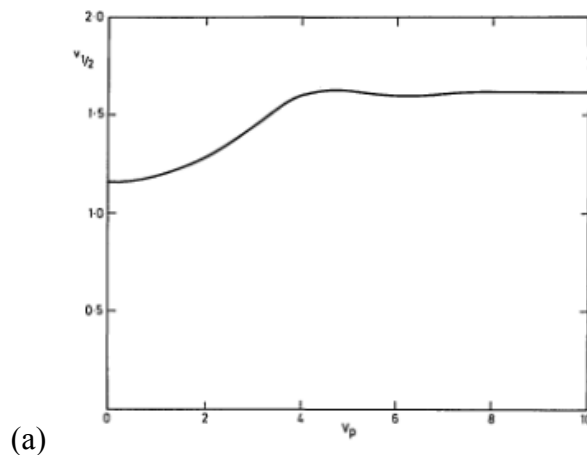
$$v = krsin\alpha \quad (11)$$

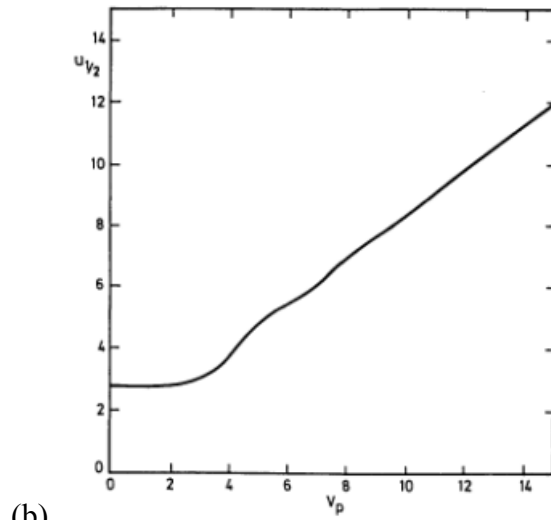
$$u = kzsin^2\alpha \quad (12),$$

where $k = 2\pi/\lambda$ (λ is the wavelength), r is the radius of the pinhole, z is the axial coordinate, and $sin\alpha$ is the numerical aperture. The numerical aperture was previously defined as the ratio D/f , where f is the focal length of the objective lens and D is the diameter of the objective lens, but it is also defined by $nsin\alpha$, where n is the index of refraction of the medium between the lens and the sample and α is half of the angular aperture of the lens [4]. In the equations above, it is assumed the medium is air, so $n = 1$. v is the normalized unit for the real radial coordinate, r , and u is the normalized unit for the real axial coordinate, z . The radius of the pinhole can also be written in normalized units, called v_p .

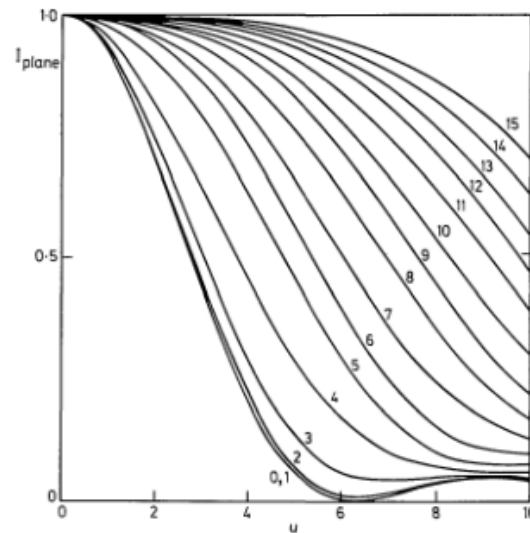
Wilson and Carlini identify how the size of the pinhole affects the width of the focal spot in the lateral and axial directions. They examine these relationships in three graphs shown in Figure 11: (a) the half width of the focal spot, or image, in the lateral

direction as a function of the radius of the pinhole in normalized units, $v_{1/2}$ vs. v_p ; (b) the half width of the image in the axial direction as a function of the radius of the pinhole in normalized units, $u_{1/2}$ vs. v_p ; and (c) the intensity of the signal as a function of axial distance for different pinholes in normalized units, I_{plane} vs. u . In Figure 11(a), it can be deduced that a pinhole less than 0.5 optical units is an appropriate size for a confocal system because the half-width of the image laterally is constant. Choosing a pinhole bigger than that might cause poor image resolution. For instance, if the pinhole size is around 4 optical units, the graph curves, indicating the resolution is poor. In Figure 11(b), the graph shows that for a pinhole size of less than 2.5 optical units the half-width of the image axially remains constant. This means the axial sectioning is the same for that range of pinholes. For pinhole sizes greater than 2.5, the half-width values increase at a relatively steady slope. Wilson and Carlini find that the lateral sectioning is more sensitive than the axial sectioning. Figure 11(c) shows that as the axial distance increases, the intensity decreases.





(b)



(c)

Figure 11: (a) The half width of the image laterally, $v_{1/2}$, as a function of the pinhole size v_p . (b) The half width of the image axially, $u_{1/2}$, as a function of v_p . (c) Intensity as a function of axial distance, u at pinhole sizes 0 to 15 [16].

The pinhole size affects the decline of intensity. With a smaller pinhole, the intensity drops at a faster rate as the axial position increases. With a bigger pinhole, this rate of decline in intensity is slower. Wilson and Carlini conclude that the pinhole size has to be at least 0.5 optical units to have a functioning confocal system. However, if a higher axial

resolution is desired, then a larger pinhole detector can be used without a significant change in lateral sectioning.

The Wilson and Carlini theory is essential to this study because it is used to confirm the confocal system is working properly. By converting various pinhole sizes to normalized units, the theoretical FWHM can be calculated. Below is a sample calculation to further explain this process. Consider a system with a pinhole of radius, $r_p = 50$ micrometers (μm), a laser with a wavelength, $\lambda = 660$ nm, a total magnification 131.9x, and a numerical aperture, $n\sin\alpha$, 0.7. First, using (11) find v_p (Note: Divide by the total magnification to get v_p in normalized units):

$$v_p = \frac{k r_p \sin\alpha}{\text{total mag}}$$

$$v_p = \frac{2\pi}{660\text{nm}} \frac{(50\mu\text{m})(0.7)}{131.9}$$

$$v_p = 2.53 .$$

Next, refer to Figure 11(b) and find the corresponding $u_{1/2}$ value for v_p . In this example, $u_{1/2} = 3.1$ when $v_p = 2.53$. So then $u = 6.2$ when $v_p = 2.53$. Using (12), solve for z , which is the FWHM in SI units:

$$u = kz\sin^2\alpha$$

$$z = \frac{u}{k\sin^2\alpha}$$

$$z = \frac{6.2}{\left(\frac{2\pi}{660\text{nm}}\right)(0.7)^2}$$

$$z = 1.33 \mu\text{m}.$$

Hence, for a pinhole with radius $50 \mu\text{m}$, the FWHM of the graph should theoretically be $1.33 \mu\text{m}$. This calculation is performed in the pages to come in the Data section, but an example is provided here to further illustrate the significance of this theory.

Axial sectioning and pinhole size are fundamental when building a confocal system. The next section addresses the theory required for characterizing the microscope. In order to understand this process, knowing how light scatters is essential. This section also explains how to choose the appropriate optical phantoms for characterization.

2.3 The Scattering of Light and the Scattering Coefficient

When examining samples under a microscope, some light will be lost due to absorption and scattering. In this study, the focus is on the relation between axial sectioning and the effective scattering coefficient of the optical phantom. The effective scattering coefficient is defined by the loss of light due to scattering and any aberrations in the system. This coefficient needs to be measured for each sample. In order to perform this measurement, it is crucial to know how light scatters. There are two types of scattering: Mie and Rayleigh scattering. Mie theory predicts the scattering of particles around the same size as the wavelength of light, while Rayleigh theory describes scattering of particles that are small compared to the wavelength. Mie scattering depends on the properties of the particles such as shape, size, and index of refraction. Mie theory applies for particles until they reach the Rayleigh limit, a limit where the particles become too small and then the scattering follows the Rayleigh theory [17]. In this study, both Mie and Rayleigh theory apply to the scattering. Scattering affects the intensity of light because it deflects light from its initial path. The Beer-Lambert Law explains this loss of light.

2.3.1 Beer-Lambert Law

The Beer-Lambert Law relates intensity of the light to the path length and attenuation coefficient:

$$I(z) = I_0 e^{-\mu z} \quad (13),$$

where z is the length of the path through the medium, I_0 is the initial intensity of the beam, and μ is the attenuation coefficient [4]. μ includes the loss of light due to both absorption and scattering. As the path length, z , through the sample increases the intensity decreases exponentially. From (13), the equation can be rearranged:

$$-\mu z = \ln \left(\frac{I}{I_0} \right) \quad (14).$$

A linear relationship is now evident in between z and $\ln \left(\frac{I}{I_0} \right)$. The equation has a slope $-\mu$. Figure 12 shows how the attenuation coefficient of a medium is measured.

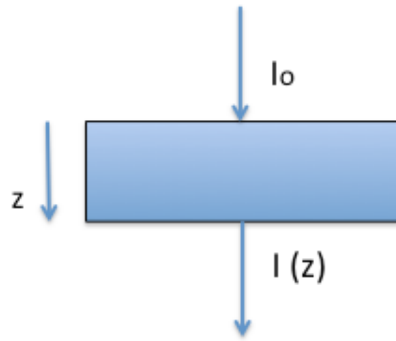


Figure 12: Beer-Lambert Law. According to the Beer-Lambert Law, intensity, I , is a function of the path length or thickness, z , of the sample. By taking a measurement of the initial intensity of the beam and the intensity of the beam after it travels through the medium, the attenuation coefficient can be calculated if the thickness of the medium is also known.

With the Beer-Lambert Law, the attenuation coefficient can be calculated when the path length and initial and final intensities of light are known. This law is useful in calculating the scattering coefficients of the optical phantoms too. If the phantom has a very low absorption coefficient, like in this study, it is assumed that the majority of the attenuation coefficient is due to scattering. So in this case, μ is the effective scattering coefficient. By

using the Beer-Lambert Law, the effective scattering coefficients of optical phantoms can easily be measured and calculated.

2.3.2 Optical Phantoms

Optical phantoms are synthetic specimens designed to mimic the optical properties of real samples. I hope to construct my own optical phantom to reproduce the structural and optical properties of human skin and tissue. A main application for optical phantoms is calibrating imaging devices. The components of phantoms can be customized to yield desired optical properties such as scattering and absorption coefficients [18]. The components of phantoms can include a scattering material, absorbers, fluorophores, and a phantom matrix material. For the scattering material, lipids or polymer microspheres can be used. Scattering materials vary in particle size and index of refraction. Some are permanent, like quartz glass microspheres, while others are not permanent, like lipids. Additionally, absorbers and fluorophores can be added to phantoms. India ink is an example of an absorber. Another example is whole blood, which might be used to achieve a realistic tissue spectrum. A phantom matrix material holds all the components of the phantom in place. This might be used to suspend the scattering material or absorber in the phantom. Gelatin, agar, and epoxy resins are some options for the phantom matrix material [18]. Because of the wide range of ingredients possible for an optical phantom, numerous of tissue samples can be mimicked.

Optical phantoms are sold commercially, but researchers can also construct their own optical phantoms. For instance, researchers, A.L. Dayton and S.A. Prahl, at Oregon Health and Science University created a turbid-polyurethane phantom to test a reflectance mode confocal microscope. In the phantom, India ink was used for the absorber, Epolin

5532 was used for the absorber, and titanium dioxide particles was used as the scattering material [19]. In another study, S.L. Jacques, B. Wang, and R. Samatham, researchers also at Oregon Health and Science University, examined three types of commercial phantoms with a reflectance confocal scanning laser microscope: polyurethane microspheres, solid polyurethane phantoms, and Spectralon™ [20]. Using a customized phantom versus a commercial phantom depends on the objective of the research.

In my research, the objective is to image an optical phantom that mimics human skin. It is more convenient and economical to create a phantom from scratch. By creating the phantom, the optical properties can easily be varied and there are more possibilities for exploration. Although customized optical phantoms allow for more creativity, there is not standardized data available. The most accurate way to verify results is to compare it with previous studies. The research done by D. Wang, Y. Chen, and J.T.C. Liu at Stony Brook University is the primary comparison for my study. They compared the properties of a liquid Intralipid optical phantom to real human skin epithelial tissue using a reflectance-based dual-axis confocal microscope. The purpose was to show this liquid optical phantom has the same scattering properties as human skin epithelial tissue [21]. Because live human tissue is not available to image, the data from the research done at Stony Brook provides the baseline for theoretical data in this paper. Hence, now that the theory of light, axial sectioning, and optical phantoms has been discussed, the next chapter goes into detail explaining the process of how this microscope was build.

3. Building the Confocal Microscope

The development of this confocal microscope involved three different setups. Challenges occurred with the first and second setup, which led to the third and final setup that performed as expected. The three setups are discussed in Section 3.2. However, before the specifics are addressed, Section 3.1 explains the equipment used in all of the stages building the microscope.

3.1 Equipment Used

This section outlines the essential equipment used in the confocal system. The defining elements of the system begin with the light source, detector, and objective lens. Throughout the changes in setup, the same light source was used, however, two detectors and two different objective lenses were utilized. Other important parts of the microscope include galvo scanners, and spatial filters.

Laser

The light source for this system is a 660 nm, 100mW laser (Obis 660LX, Coherent, Santa Clara, CA [22]). This is a diode laser or semiconductor laser. Diode lasers are made of semiconductors, such as gallium arsenide, and are doped to form a p-n junction like a typical diode [23]. The p-n junction causes electrons to flow because the p side has the holes the electrons on the n side want to fill. The p side has a slight negative charge and the n side has a slight positive charge. When the electrons transfer to the holes, a photon is emitted. Mirrors are inside the junction and as more electrons transfer more photons accumulate and bounce off of the mirrors together. When enough photons have been produced, they go through a photodiode to regulate voltage. A photodiode in the p-n junction functions as a light meter [24]. The photons go through a lens and the

laser beam is produced [25]. This laser takes less than five minutes to warm up and the diameter of the beam is 0.9 mm. Lasers are classified into categories I to IV, where Class I lasers are the safest and Class IV lasers are high emitting and hazardous [26]. This laser is in Class IIIB, meaning it is of medium power and can damage the eyes if looked at directly.

Detectors

There were two photodetectors used in this microscope. Photodetectors convert light into current. The first detector, and ultimately the one used in the final setup, is the Large Area Mounted Silicon Photodiode (SM05PD1A, Thorlabs Inc., Newton, NJ [27]). It has a wavelength range from 350 to 1100 nm. The second detector is the Si Variable-Gain Avalanche Photodetector (APD410A, Thorlabs Inc. [28]). This kind of detector only responds to AC currents. It is used in applications that require high accuracy and low-level light detection [29]. The second detector was utilized in Setup II when the detector signal was incredibly low. It could collect much lower signals than the first detector because it has a higher sensitivity level. It also has continuous variable gain with an M factor from 10 to 100 and an output bandwidth of DC to 10 MHz. Its wavelength range is from 400 nm to 1000 nm. The second detector is not used in the final design, Setup III, because the high sensitivity level is not required. A third detector that will be used in the future is the ADP Module Avalanche Photodiode (C12702-12, Hamamatsu, Japan [30]). This kind of detector only responds to high frequency signals. This detector will be needed when the microscope can scan the sample with mirrors and build the image with computer software.

Objective Lenses

Objective lenses are characterized by their magnification, numerical aperture, and the medium between the front lens and sample. The numerical aperture is a value that describes the microscope's ability to collect light and resolve the specimen [31]. Possible mediums for objective lenses are air, water, and oil. The two types used with this system were a 20x, 0.7 numerical aperture air immersion lens (UCPLFLN, Olympus, Waltham, Massachusetts [32]) and a 60x, 1.42 numerical aperture oil immersion lens (PLAPON, Olympus [33]). For the air immersion objective lens, the working distance is 0.8-1.8 mm. This lens also has a correction collar to account for cover glass thickness. Often air objective lenses experience spherical aberrations due to the cover glass [34]. This collar helps reduce these aberrations by adjusting to the thickness of the cover glass.

The oil immersion objective lens has a working distance of 0.15 mm. This lens does not have a correction collar and works with cover glass 0.17 mm thick. The medium between the front lens and sample is oil (Immoil-F30CC, Olympus [35]). The oil has an index of refraction 1.518. The oil objective lens was used in the second setup, but unfortunately did not work out. Therefore, the air objective lens is used the final setup.

Galvanometer Scanners

Galvanometric or galvo scanners serve the important role of guiding the beam over the sample. There were two galvo scanners in the first and second setups: a large scanner (GVS211, Thorlabs [36]) and a small scanner (GVS201, Thorlabs [37]). The galvo scanners are controlled by the polarity of the current. The mirrors are on limited rotation DC motors that rotate depending on the amount of voltage given. The polarity of the current determines the direction of the rotation. Increasing the voltage increases the speed of the scanners. Galvo scanners have the ability to scan a specimen in the x and y

direction [38]. For instance, they can perform a saw-tooth scan (raster scan), where the laser moves over the sample left to right and then moves back to the left and lower to repeat. Another type of scan is the bidirectional scan, where the laser records in both the x and y directions. With galvo scanners, one has complete control over the laser, so it can scan in specific patterns as well. Also, this type of scanner is excellent with slow scans, around a half a frame a second, because it can pick up great detail that is needed in structural experiments [39]. Galvo scanners are used for experiments that focus more on morphological imaging or structural development, where high resolution is critical and the scanning speed can vary. Unfortunately due to problems in Setup II, the galvo scanners are not in Setup III. Without the scanners, the microscope cannot scan an actual sample; however, imaging a sample is beyond the scope of this study. The microscope can still be characterized with optical phantoms, and later the scanners can be incorporated into future designs.

Spatial Filters and Irises

There are multiple irises and one spatial filter in the microscope to shape the beam. The laser beam should ideally be a beautiful round Gaussian beam. However, lasers often experience spatial noise from the scattering of particles and optical imperfections. This is why spatial filters and irises are incorporated into the beam path. They help reduce intensity inconsistencies by blocking out the additional noise. A spatial filter has a pinhole of a certain diameter that allows only the focus of the source to pass through. It is possible to calculate the appropriate size of the spatial filter for a microscope using the equations:

$$D_B = \frac{1.27\lambda f}{D} \quad (15)$$

$$D_P = 1.5 D_B \quad (16),$$

where λ is the wavelength of the laser, f is the focal length of the objective lens, D is the diameter of the original beam, D_B is the diameter of the beam spot, and D_P is the diameter of the pinhole [9]. For instance, in this microscope $\lambda = 660 \text{ nm}$, $f = 9 \text{ mm}$, $D = 0.9 \text{ mm}$. So:

$$D_B = \frac{1.27(660 \text{ nm})9\text{mm}}{0.9\text{mm}}$$

$$D_B = 8.38 \mu\text{m}$$

Then,

$$D_P = (1.5)(8.38 \mu\text{m})$$

$$D_P = 12.5 \mu\text{m}$$

So the ideal size of the spatial filter for the microscope is 12.5 microns. A spatial filter blocks noise from continuing on; hence, the intensity and shape of the beam becomes more consistent. A crucial step when using a spatial filter is maximization, which involves adjusting its position so the greatest amount of light can travel through. If not enough light is passing through, this may result in poor resolution. Maximizing the spatial filter is extremely important for a correctly functioning microscope.

3.2 Methods

Now that a brief description of the equipment has been given, this section explores the evolution of the microscope, the challenges I encountered and how I either overcame them or choose a different path to embark on. I investigated three separate setups. The objective for each setup was to compare its axial sectioning with the Wilson and Carlini theory to determine if the system was working properly. The problems that

arose in the first and second setups are outlined, as well as the successes with the third setup.

3.2.1 Setup I

The total magnification of the first set up was 66.6x with the air immersion objective lens. The setup is shown in Figure 13. I soon experienced challenges with alignment and collimation of the beam. Alignment involved adjusting the beam expanders so the beam was collimated after each one. It also included maximizing the spatial filter and wave plates. The half and quarter wave plates dictate the polarization of the beam by changing the light to one orientation. I used small targets to center the beam on the lenses, index cards to check for side and back reflections, and irises to level the beam on the vertical part. However, the beam could never be successfully collimated because of alignment issues.

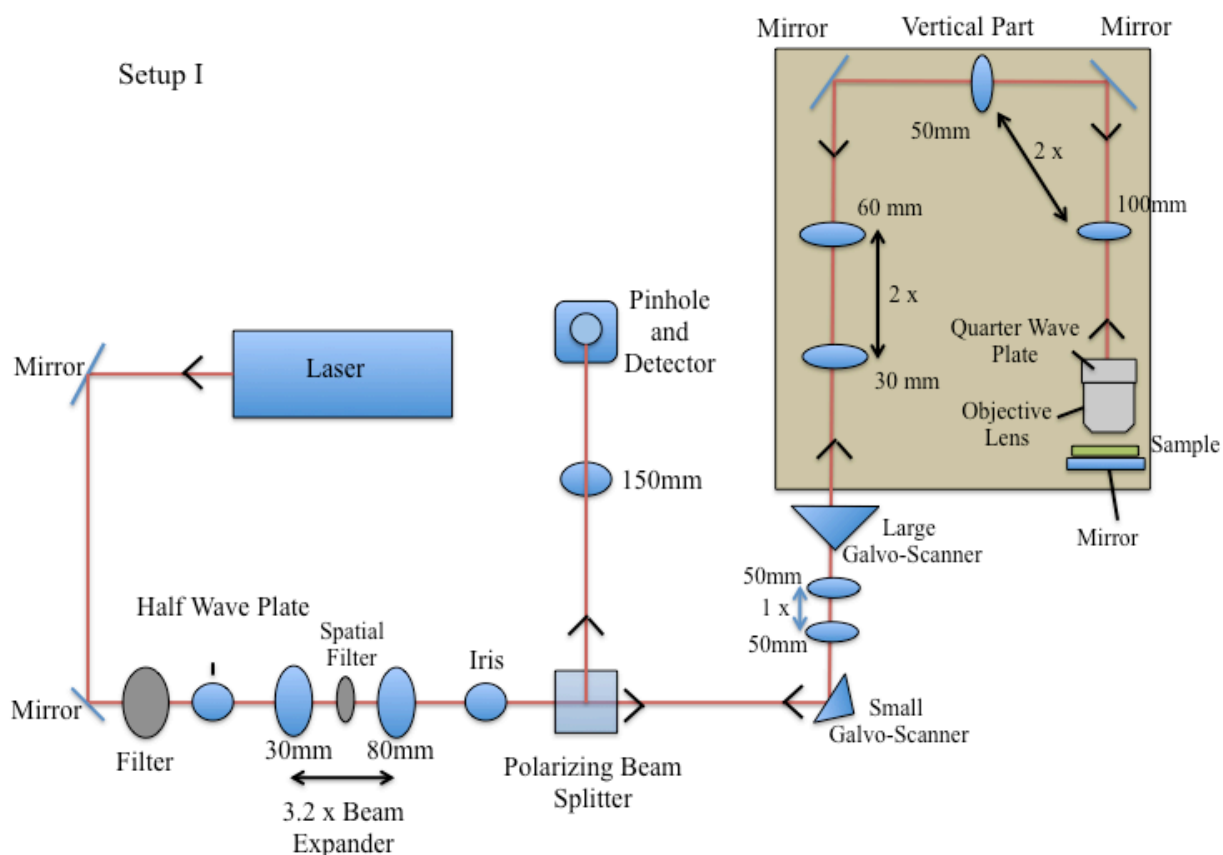


Figure 13: Setup I. This is the schematic for Setup I of the microscope. The incoming beam travels through the system and sample, and reflects off of the mirror. The reflected beam retraces the path through the polarizing beam splitter and then goes through the pinhole to the detector.

Another problem with this setup was the position of the scanners. Aligning the scanners is an iterative process where the correct distance between them needs to be found. To align them, I applied voltage to the first scanner and then placed the second scanner in the location where the beam was stationary. Then I applied voltage to the second scanner and adjusted the first scanner accordingly so the beam was stationary on it. Appropriate positions for the scanners (where the beam was stationary on both) were never found most likely due to the alignment problems. I could not test the system's axial sectioning because of the many challenges with alignment. Consequently, in the hopes to minimize these complications, I chose to pursue a new setup.

3.2.2 Setup II

For Setup II, I reduced the number of beam expanders and repositioned the scanners. The setup is shown in Fig. 14. The 1x beam expander was removed from the horizontal section and the scanners were relocated to the vertical part. For alignment, I removed the entire vertical section from the system and aligned it backwards with a He-Ne laser on a separate table.

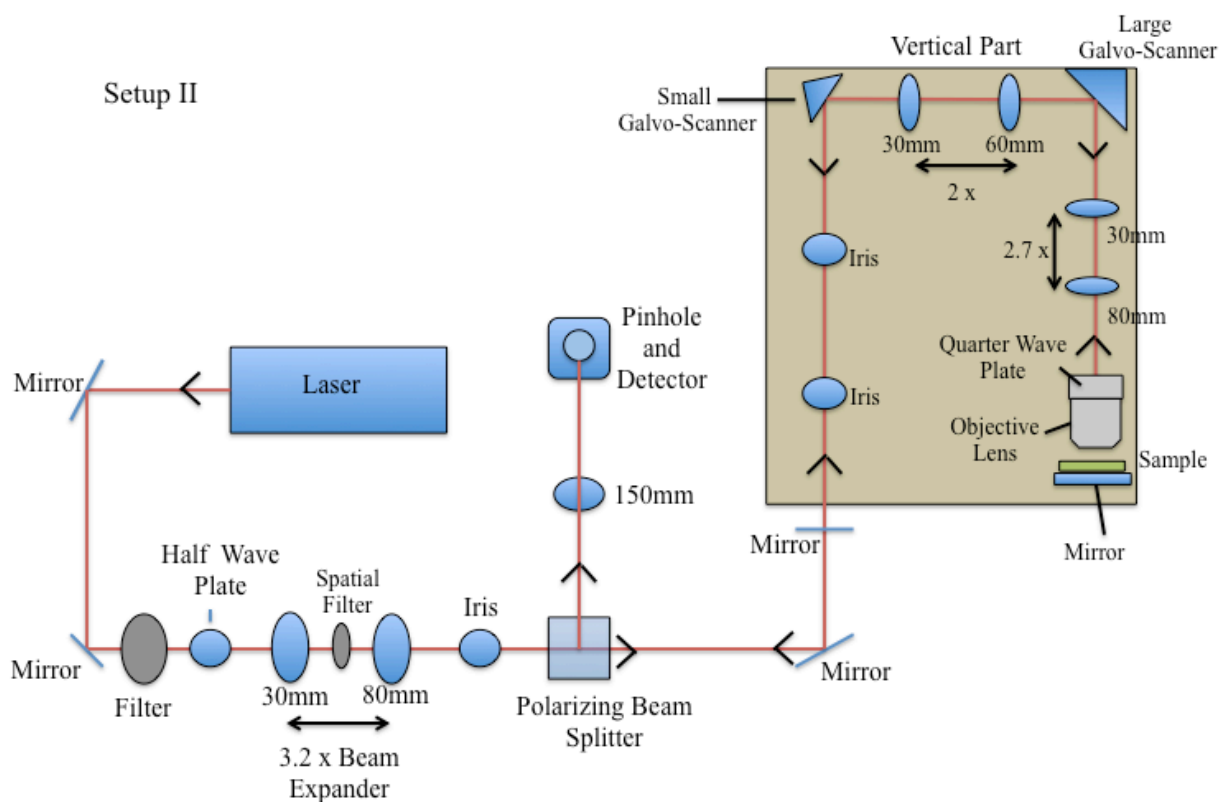


Figure 14: Setup II. This is the second schematic of the confocal microscope. It has fewer beam expanders and the scanners are both on the vertical part. These modifications were made to simplify the system and make it easier to align.

The beam ran through the system as if it was the reflected returning beam. This method of alignment was easier because it allowed more visibility and access to the lenses and scanners. The total magnification of Setup II was 88.8x with the air objective lens. These adjustments I made resulted in correct alignment and collimation of the beam. The next

step was to determine the microscope's axial sectioning and compare it with the Wilson and Carlini theory.

Axial Sectioning: Air Lens

I calculated the theoretical FWHM for the system for three pinhole diameters: 100, 150, and 200 μm . Recall that Setup II had a laser with a wavelength, λ , 660 nm, a total magnification 88.8x, and a numerical aperture $n\sin\alpha = 0.7$. For the 100 μm pinhole, the radius, r_p , is 50 μm . I used equation (11) from Section 2.2:

$$v_p = \frac{k r_p \sin\alpha}{\text{total mag}}$$

$$v_p = \frac{\frac{2\pi}{660\text{nm}}(50\ \mu\text{m})(0.7)}{88.8}$$

$$v_p = 3.75 .$$

Then, I referred to Figure 11(b). I used a program called ImageJ, which estimates the values on the graph better than the naked eye. ImageJ uses the pixels in the image and a set scale of the graph to estimate the values. The corresponding $u_{1/2}$ value for $v_p = 3.75$ is $u_{1/2} = 3.67$. So then $u = 7.34$. Lastly, I used equation (12) and solved for z , which is the FWHM:

$$u = kz\sin^2\alpha$$

$$z = \frac{u}{k\sin^2\alpha}$$

$$z = \frac{7.34}{\left(\frac{2\pi}{660\text{nm}}\right)(0.7)^2}$$

$$z = 1.57\ \mu\text{m}.$$

Therefore, the FWHM for the 100 μm pinhole is 1.50 μm . I performed the same calculations for the 150 and 200 μm pinholes. The results are summarized in Table 1.

Pinhole Diameter Size (μm)	v_p	$u_{1/2}$	u	z (μm)
100	3.75	3.67	7.0	1.57
150	5.63	5.48	10.96	2.35
200	7.50	6.77	13.54	2.90

Table 1: Results of FWHM Calculations for Pinholes 100, 150, and 200 μm Using the Air Lens.

From these theoretical calculations, I observed that as the pinhole size increased, the FWHM increased as well. As mentioned in Section 1.2 and explained in Figure 6(a), axial sectioning data is collected when the sample moves through the focal plane. In this case, the mirror acted as the sample. I adjusted the detector position until the optimal axial sectioning was reached, meaning the experimental FWHM value was approximately the theoretical value. Ideally, the distance between the detector and detector lens should be around the focal length of the detector lens. Since the detector lens had a focal length of 150 mm, the detector was approximately 150 mm away from the detector lens. I collected axial sectioning data for each pinhole and then graphed the detector signal as a function of the sample's axial position. Five trials for each were done and then averaged to find the experimental FWHM. Figure 15 displays the averaged axial sectioning data graphs.

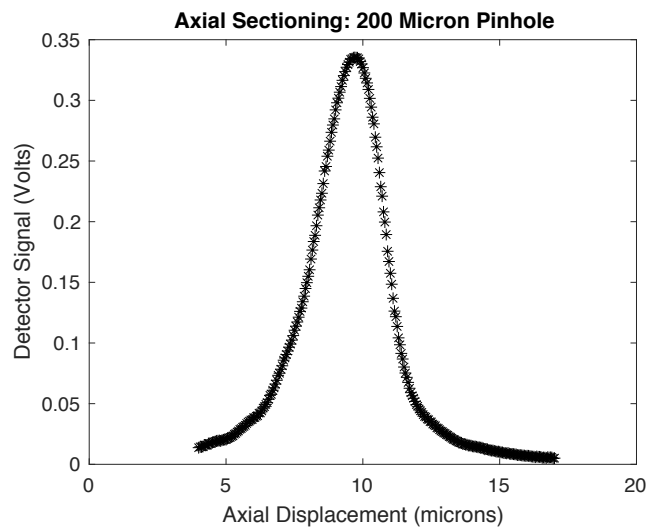
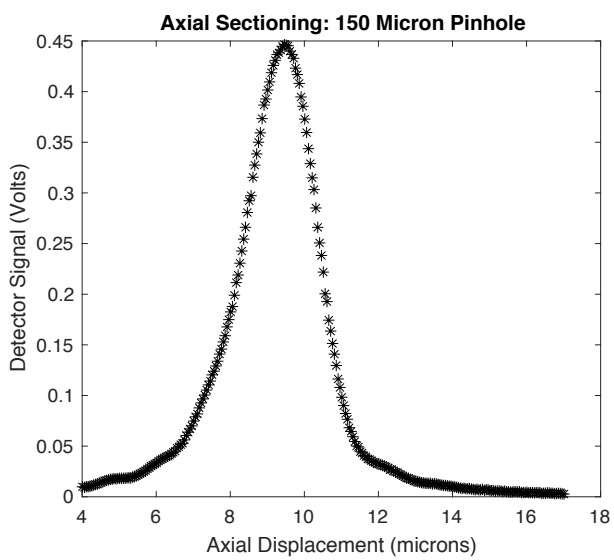
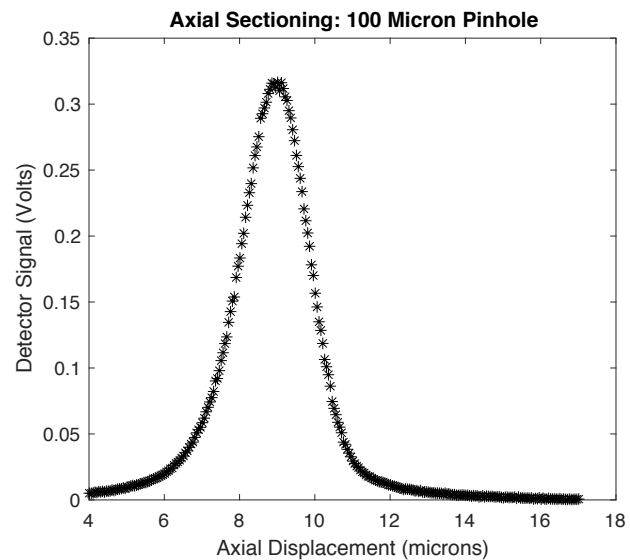


Figure 15: Averaged Axial Sectioning Graphs for Pinholes 100, 150, and 200 μm . Five trials were run for each pinhole. These graphs are the average of the five trials.

The experimental FWHM values were accurate compared to the theoretical values. Table 2 shows the comparison.

Pinhole Diameter Size (μm)	Theoretical FWHM	Experimental FWHM \pm std. dev.	Percent Difference %
100	1.57	$1.79 \pm 1.5\%$ (n=5)	+11%
150	2.35	$2.25 \pm 0.7\%$ (n=5)	-5%
200	2.90	$2.86 \pm 1.6\%$ (n=5)	-2%

Table 2: Theoretical FWHM vs. Experimental FWHM for 100, 150, 200 μm Pinholes

The experimental values had a low percent error when compared to the theoretical values for all of the pinholes. This data matched the Wilson and Carlini theory and showed that the confocal system was working properly. Given this success, another objective lens was tested with this system.

Axial Sectioning: Oil Lens

I next tested the axial sectioning of the system with the oil immersion lens to see if that could yield equally successful results. I switched the detector lens from a 150 mm to a 100 mm lens, so the magnification of the microscope would not be too large. With the oil lens and 100 mm detector lens, the total magnification of the system was 177.8x. I used water as the sample because this medium does not contain any scattering material. The axial sectioning when imaging through water provides the initial data and later is compared with the axial sectioning of the system when imaging through the optical phantoms. The sample mounting is shown in Figure 16.

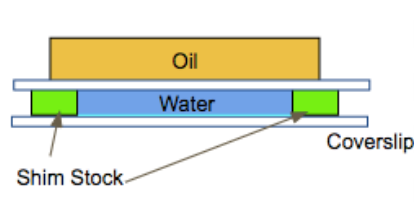


Figure 16: Bridge Method for Water Sample Mounting With Oil Lens. The bridge method was used to mount the sample. Two pieces of shim stock were placed on a coverslip and then a drop of water was put in between the shim stock. The purpose of the shim stock is to control the thickness of the sample. Another cover slip was placed on top. When using the oil lens, there needs to be a drop of oil on the top of the coverslips, so the lens can be immersed in the oil while imaging.

Using the information of Setup II ($\lambda = 660$ nm, total magnification 177.8x, and numerical aperture 1.42) and the equations (11) and (12), I calculated the theoretical FWHM for three pinholes. The results are shown in Table 3.

Pinhole Diameter Size (μm)	v_p	$u_{1/2}$	u	z (μm)
100	3.80	3.71	7.42	0.387
150	5.70	5.48	10.96	0.571
200	7.60	6.92	13.84	0.721

Table 3: Results of FWHM Calculations for Pinholes 100, 150, and 200 μm Using Oil Lens.

I found that the theoretical FWHM values with the oil lens were smaller than the theoretical FWHM values with the air lens because of the change in numerical aperture. An example of the axial sectioning data graphs for imaging through water with the oil lens is displayed in Figure 17. The axial sectioning graphs all looked similar to the graph shown below. Unlike the expected smooth Gaussian curve, this graph had multiple peaks and was extremely noisy. The multiple peaks typically indicated the detector was off in the horizontal and vertical directions. However after further adjustments, the peaks would still not disappear.

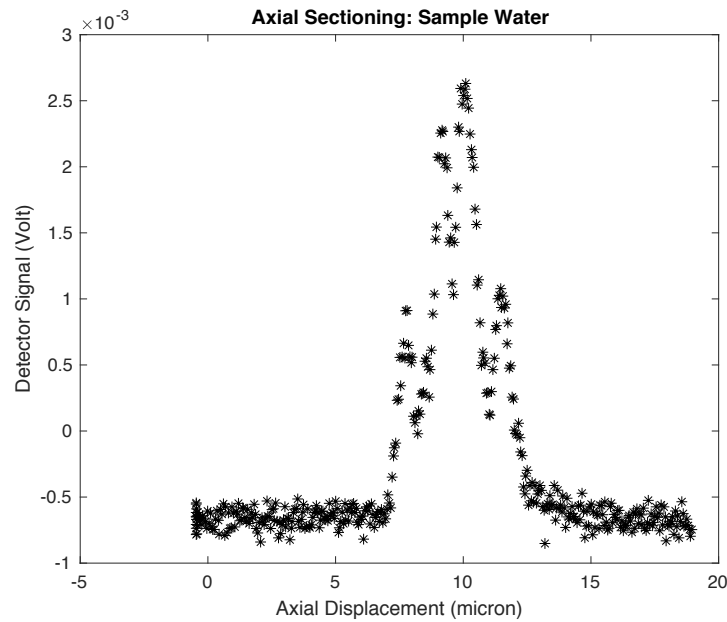


Figure 17: Axial Sectioning Graph for 100 μm Pinhole With Water Sample.

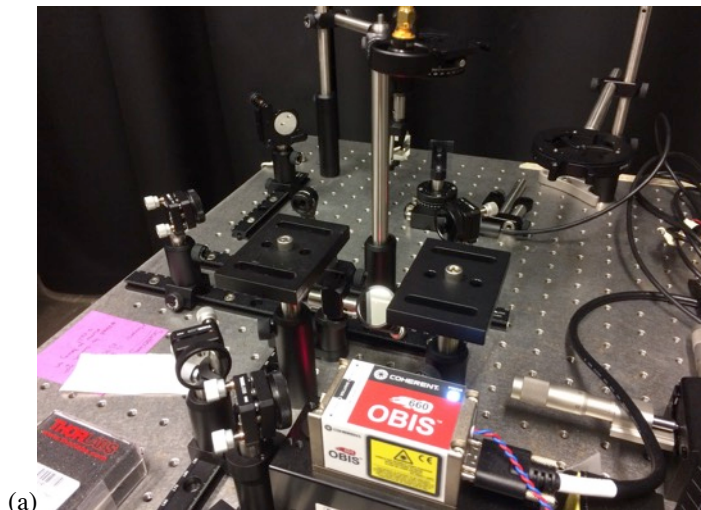
Another cause for this peculiar graph could be a misaligned system. I discovered that due to either shifts or unintentional bumps the beam was misaligned on the vertical section. Instead of realigning the entire section, I removed the 2x and 2.7x beam expanders. More axial sectioning data was collected, yet the graphs still were incredibly noisy. The detector signal was too low for the Large Area Mounted Silicon Photodiode to handle. To solve this problem, a Si Variable-Gain Avalanche Photodetector was ordered. During the wait for the new detector, I began to investigate possible optical phantoms that mimic human skin.

Optical Phantoms: Milk and Water Mixture

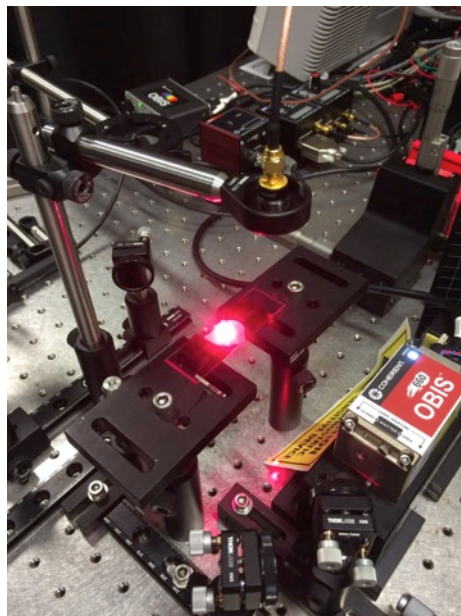
According to a biological review, human skin has a scattering coefficient ranging roughly from 30 to 70 cm^{-1} [40]. The sample used in the study by D. Wang, Y. Chen, and J.T.C. Liu at Stony Brook University was human epithelium, which has a thickness approximately 75 to 125 μm [21]. With the goal of mimicking these properties, I created optical phantoms from a mixture of milk and water. I chose milk as the scattering

material because of its success in a study done at Miami University. Researchers used milk to mix a highly turbid media. They measured the index of refraction and discovered that the attenuation coefficient was between 40 to 125 cm^{-1} , which in the desired range for human skin [15]. Milk was also easily accessible and inexpensive.

Three optical phantoms were mixed from whole milk and water: 50%, 66%, and 83% diluted mixture. Using the Beer-Lambert Law, I measured and calculated the scattering coefficient for each optical phantom. The apparatus used to collect the measurements is presented in Figure 18(a).



(a)



(b)

Figure 18: (a) Apparatus for Scattering Coefficient Measurements (b) Measuring Optical Phantom

Using the same laser for the microscope, I placed a mirror to redirect the beam towards the scattering apparatus. Another mirror reflected the beam upwards in between two posts that would hold the sample. The Large Area Mounted Silicon Photodiode suspends above the sample to measure the intensity of the beam. Figure 18(b) shows the intensity being measured after the beam travels through the sample. Recall that if the initial intensity of the beam, I_0 , the intensity after the beam travels through the medium, I , and the thickness or path length of the sample are known, the scattering coefficient can be calculated. I measured the initial intensity of the beam going through just the coverslips. Then I mounted the sample of milk mixture using the bridge method, like in Figure 19.

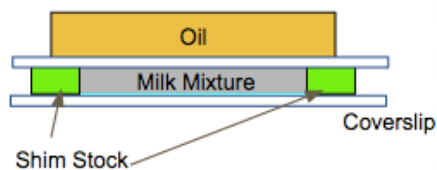


Figure 19: Bridge Method for Mounting Optical Phantom Samples With Oil Lens. This is the same mounting as the water sample. This method was used to control thickness.

The bridge method is important because it allowed the thickness of sample to be controlled. Four different shim stocks with varying thicknesses were used: 12.7, 25.4, 50.8, and 76.2 μm . I placed the sample on the posts in the laser's path and then waited 5 to 10 minutes to allow the mixture to settle. Lastly, I recorded the intensity of the beam. This process was repeated for every shim stock thickness. To assure accuracy, three trials were done for each. The trials were then averaged to get an averaged I_0 and averaged I . Table 4 displays the data collected for scattering coefficient measurements.

50% Solution									
z	I ₀	Trial One: I	Trial Two: I	Trial Three: I	Avg I	ln(I/I ₀)			
12.7	565	550	538	536	541.3333333	-0.042790499			
25.4	565	531	520	515	522	-0.079158143			
50.8	565	515	448	526	496.3333333	-0.129577987			
76.2	565	509	472	463	481.3333333	-0.1602657			
66% Solution									
z	Trial One: I ₀	Trial One: I	Trial Two: I ₀	Trial Two: I	Trial Three: I ₀	Trial Three: I	Avg I ₀	Avg I	ln(I/I ₀)
12.7	550	545	560	553	560	552	556.666667	550	-0.0120483
25.4	556	523	560	531	555	545	557	533	-0.0440438
50.8	565	498	560	515	560	536	561.666667	516.333333	-0.084156
76.2	557	478	560	465	560	488	559	477	-0.158633
83% Solution									
z	Trial One: I ₀	Trial One: I	Trial Two: I ₀	Trial Two: I	Trial Three: I ₀	Trial Three: I	Avg I ₀	Avg I	ln(I/I ₀)
12.7	558	538	558	548	556	540	557.333333	542	-0.0278975
25.4	556	511	556	527	553	527	555	521.666667	-0.0619393
50.8	556	508	560	501	560	520	558.666667	509.666667	-0.0917961
76.2	565	486	558	492	560	480	561	486	-0.1435123

Table 4: Effective Scattering Coefficient Measurements for 50%, 66%, and 83% diluted solution optical phantoms. This table shows the measurements and averaged measurements, where z is the shim stock thickness in μm , I_0 is the initial beam intensity in millivolts, and I is the beam intensity after the sample in millivolts. This table was made using Microsoft Excel.

To further explain this table, consider the 66% solution with the 12.7 μm thickness. The beam voltage, I_0 , through the coverslips was 550 mV. The 66% solution was then placed on the apparatus and the voltage of the beam was measured to be 545 mV. These measurements were repeated two more times with new coverslips and samples each time. The average of the three trials for I_0 was 556.7 mV and for I was 550 mV. Lastly, the natural logarithm of the ratio of the averaged I to I_0 was calculated:

$$\ln\left(\frac{550}{556.7}\right) = -0.012.$$

This value is important because, as seen in equation (14) in Section 2.3.1, the scattering coefficient, μ , is found when $\ln(I/I_0)$ is graphed as a function of thickness, z . I applied this calculation to every optical phantom for each thickness. Therefore, as shown in the table, a value for $\ln(I/I_0)$ existed for every thickness. Figure 20 further illustrates this relationship. Each line represents an optical phantom and the slope of the line is the scattering coefficient (it is really $\frac{|slope|}{10^{-6}}$). As seen in Figure 20, for the 50% solution $\mu = 18 \text{ cm}^{-1}$, for the 66% solution $\mu = 17 \text{ cm}^{-1}$, and for the 83% solution $\mu = 22 \text{ cm}^{-1}$.

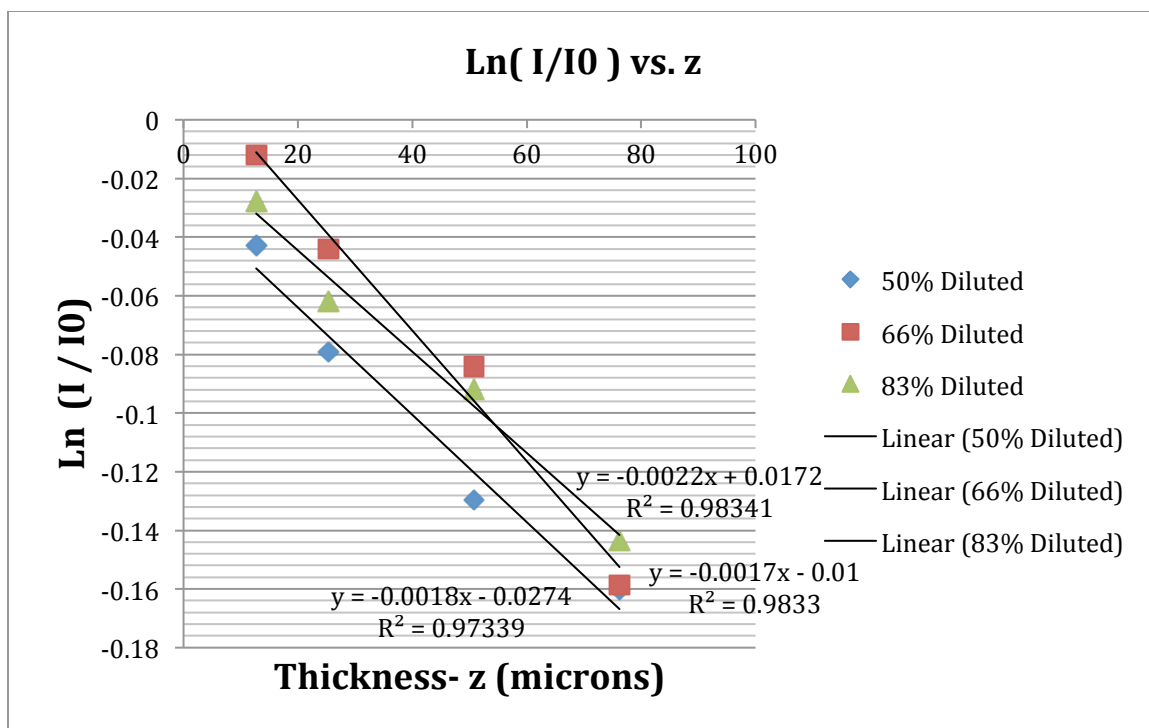


Figure 20: $\ln(I/I_0)$ vs. z for 50%, 66%, and 83% Diluted Solutions. The absolute value of the slopes of the lines are the scattering coefficients.

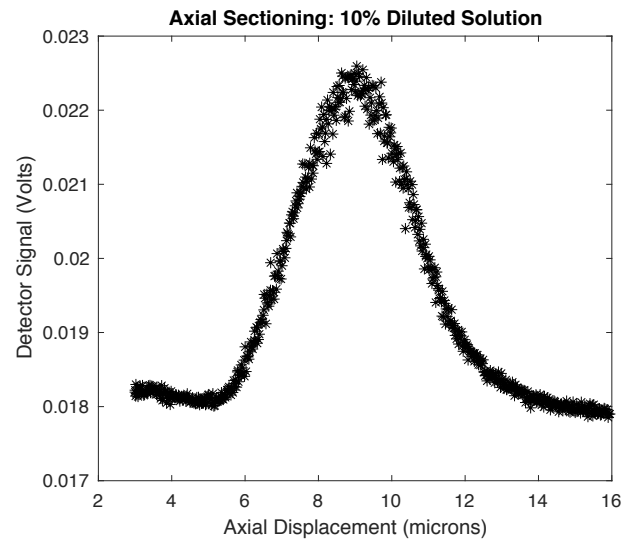
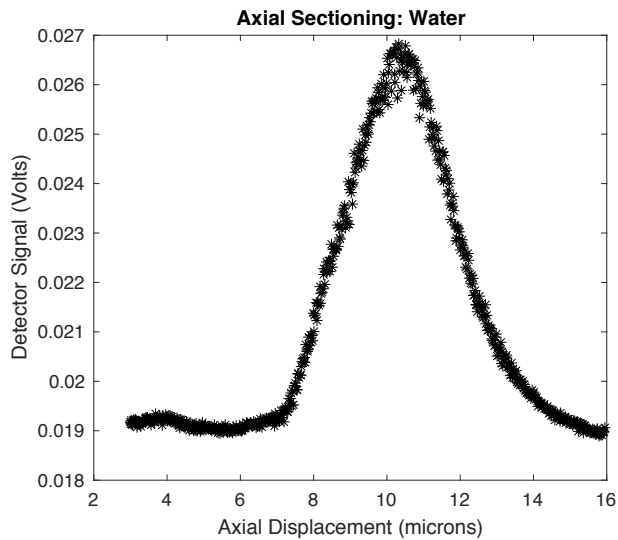
Unfortunately, these optical phantoms had scattering coefficients out of the range for human skin. Another problem was the values were all similar. I expected that as the optical phantom had more scattering material the μ would increase; yet these results did not support this. Despite the fact that these optical phantoms did not mimic the properties of human skin, I established a method for finding the scattering coefficients. By this time, the new detector had arrived. I could now start to image optical phantoms.

Characterization of the Microscope

The new Si Avalanche Photodetector solved the issue of the low signal because it could detect the signal with its high sensitivity. The axial sectioning for water with the oil lens was now not as noisy and the graphs were nice Gaussian Curves. However, there still remained a fundamental problem with the axial sectioning because the experimental FWHM values did not match the theoretical FWHM values for the respective pinholes.

Despite trying all of the possible detector positions, the FWHM was still larger than the theoretical FWHM for water. The cause of this difference was unknown. Nonetheless, I proceeded and started to image through optical phantoms with the microscope to observe how the scattering material affected the FWHM for water, even though it was inaccurate. My hypothesis was as the amount of scattering material increased in the phantom, the FWHM should increase too. The optical phantoms I previously tested lied out of the desired range for the scattering coefficient. Therefore, I tried a 10%, 30%, and 50% diluted mixture of milk and water. Figure 21 shows the initial axial sectioning water data compared with the optical phantom data.

(a)



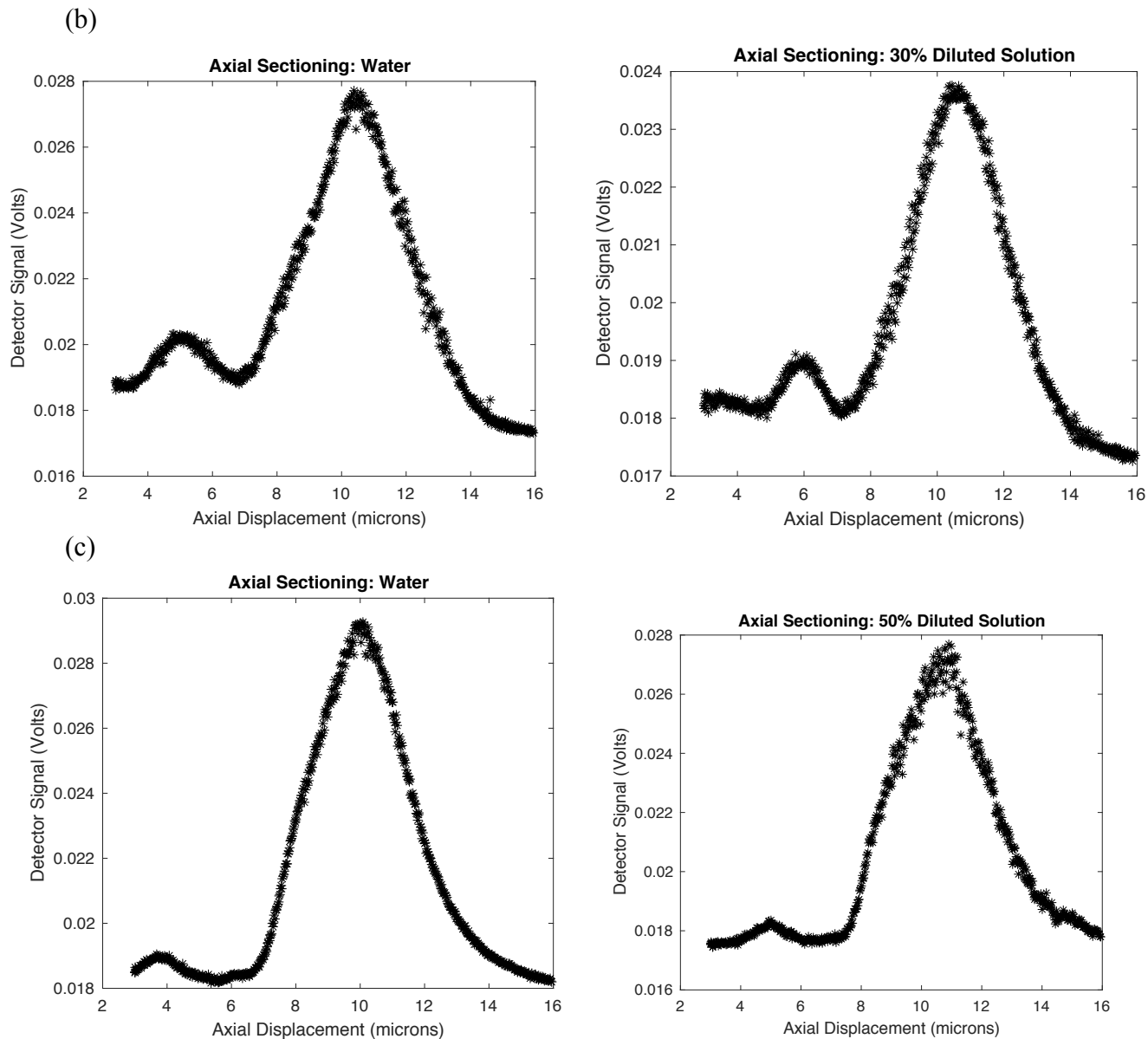


Figure 21: (a) Axial Sectioning Data of Water Compared with 10% Diluted Solution. (b) Axial Sectioning Data of Water Compared with 30% Diluted Solution. (c) Axial Sectioning Data of Water Compared with 50% Diluted Solution. All of the graphs are the average of five trials.

I took five trials of water for the initial measurement of the FWHM. Five trials were also collected for each optical phantom. Each graph shown in Figure 21 is an average of five trials. As seen in the figure, the data did not align with the hypothesis. There was not a

clear relationship between the water and optical phantoms FWHM. This is more clearly expressed in Table 5.

Optical Phantom Mixture	Water FWHM (microns)	Optical Phantom FWHM (microns)	Percent Difference %
10%	$2.96 \pm 4.5\%$ (n=5)	$3.46 \pm 7.1\%$ (n=5)	+16.9%
30%	$3.4202 \pm 3.2\%$ (n=5)	$3.02 \pm 9.0\%$ (n=5)	-11.7%
50%	$3.52 \pm 0.6\%$ (n=5)	$3.02 \pm 12\%$ (n=5)	-14.2%

Table 5: Comparison of FWHM of Axial Sectioning of Water vs. Optical Phantoms.

Because water did not have any scattering material, the water FWHM should be smaller than the optical phantom FWHM. For the 10% mixture, the FWHM increased as expected. Yet for the 30% and 50% mixture, the curve became smaller with the optical phantom. Also, the water FWHM was not consistent. The water FWHM should be around the same value for all three optical phantoms, but widely ranged from 2.96 to 3.52. These results were inconsistent and did not match with the original hypothesis. Unfortunately due to the inaccurate axial sectioning and the inconsistent data when imaging the optical phantoms, I could not progress with Setup II. Because of the limited amount of time remaining, I designed a third setup.

3.2.3 Setup III

In the final setup, I resorted back to the basics of confocal microscopy. In the previous two setups, I experienced challenges with the system alignment and inconsistent data. Setup III was more simplified, however, my main goal was to correct the errors in the previous setups and build a correctly working microscope. The magnification of this setup was 46.3x and the objective lens was switched back to the air lens. The detector signal was strong and so the original detector was used in order to not saturate the new sensitive detector. The setup is shown in Figure 22.

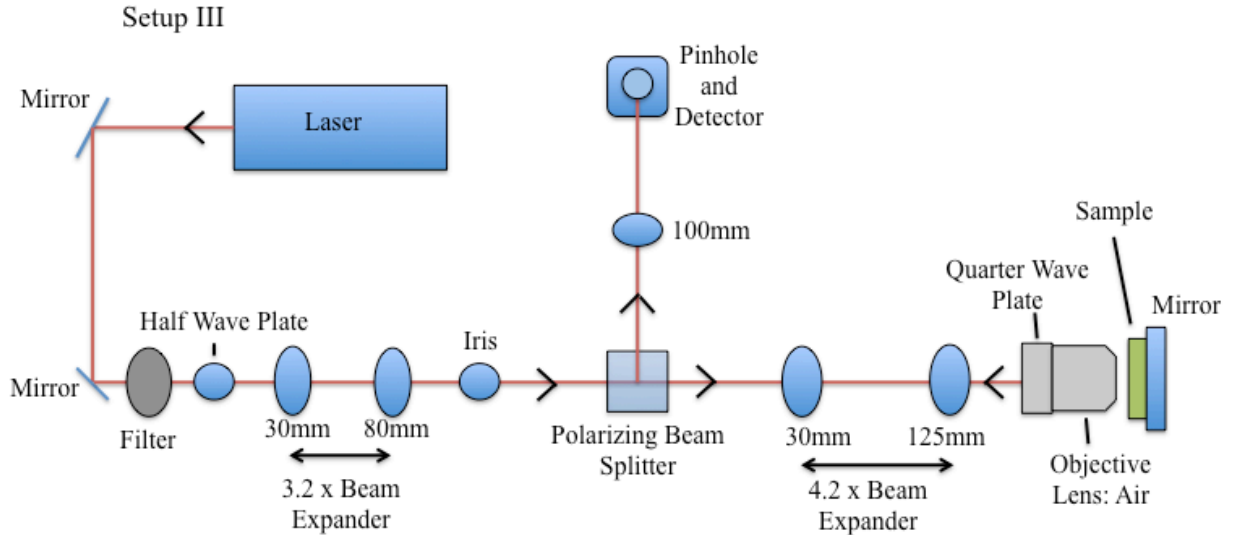


Figure 22: Setup III. The third setup has fewer components and is more simplified than the other setups.

I removed the galvo-scanners and whole vertical part. After the polarizing beam splitter, I added a 4.2x beam expander to enlarge the beam so it filled the entire pupil of the objective lens. It is important to fill the pupil to get the correct numerical aperture of the objective lens. If the pupil is not fully filled then this can lead to problems with axial sectioning. Alignment with this system was more consistent, most likely because there were fewer elements to work with. Similar to the process of the previous setups, Setup III needed to be compared with the Wilson and Carlini theory. I calculated the FWHM for five pinholes: 15, 30, 40, 50, and 100 μm . (This system had a laser with a wavelength, λ , 660 nm, a total magnification 46.3x, and a numerical aperture, $\sin\alpha$, 0.7.) For the 15 μm pinhole, the radius, r_p , is 7.5 μm . Again, I used equation (11) from Section 2.2:

$$v_p = \frac{k r_p \sin\alpha}{\text{total mag}}$$

$$v_p = \frac{2\pi}{660\text{nm}} \frac{(7.5\mu\text{m})(0.7)}{46.3}$$

$$v_p = 1.07 .$$

Referring to Figure 11(b), the corresponding $u_{1/2}$ value for $v_p = 1.07$ is $u_{1/2} = 2.9$. So then $u = 5.8$. Lastly, I used equation (12) and solved for z , which is the FWHM:

$$u = kz \sin^2 \alpha$$

$$z = \frac{u}{k \sin^2 \alpha}$$

$$z = \frac{5.8}{\left(\frac{2\pi}{660\text{nm}}\right) (0.7)^2}$$

$$z = 1.24 \mu\text{m}.$$

Therefore, the FWHM for the $15\mu\text{m}$ pinhole is $1.24 \mu\text{m}$. I performed the same calculations for the other pinholes. The results are summarized in Table 6.

Pinhole Diameter Size (μm)	v_p	$u_{1/2}$	u	z (μm)
15	1.07	2.89	5.78	1.24
30	2.15	2.94	5.88	1.26
40	2.87	3.10	6.20	1.33
50	3.59	3.46	6.92	1.48
100	7.18	6.11	12.22	2.62

Table 6: Results of FWHM Calculations for Pinholes 15, 30, 40, 50, and $100 \mu\text{m}$ Using Air Lens.

I observed that as the pinhole size increased, the FWHM increased as well, meaning the curve got wider. I took axial sectioning data for all of the pinholes and the graphs are displayed in Figure 23. Each graph is an average of three trials. The experimental FWHM values are compared with the theoretical values in Table 7. It is observed that as the pinholes increased, the curves generally grew wider. The experimental values reasonably agreed with the theoretical predictions.

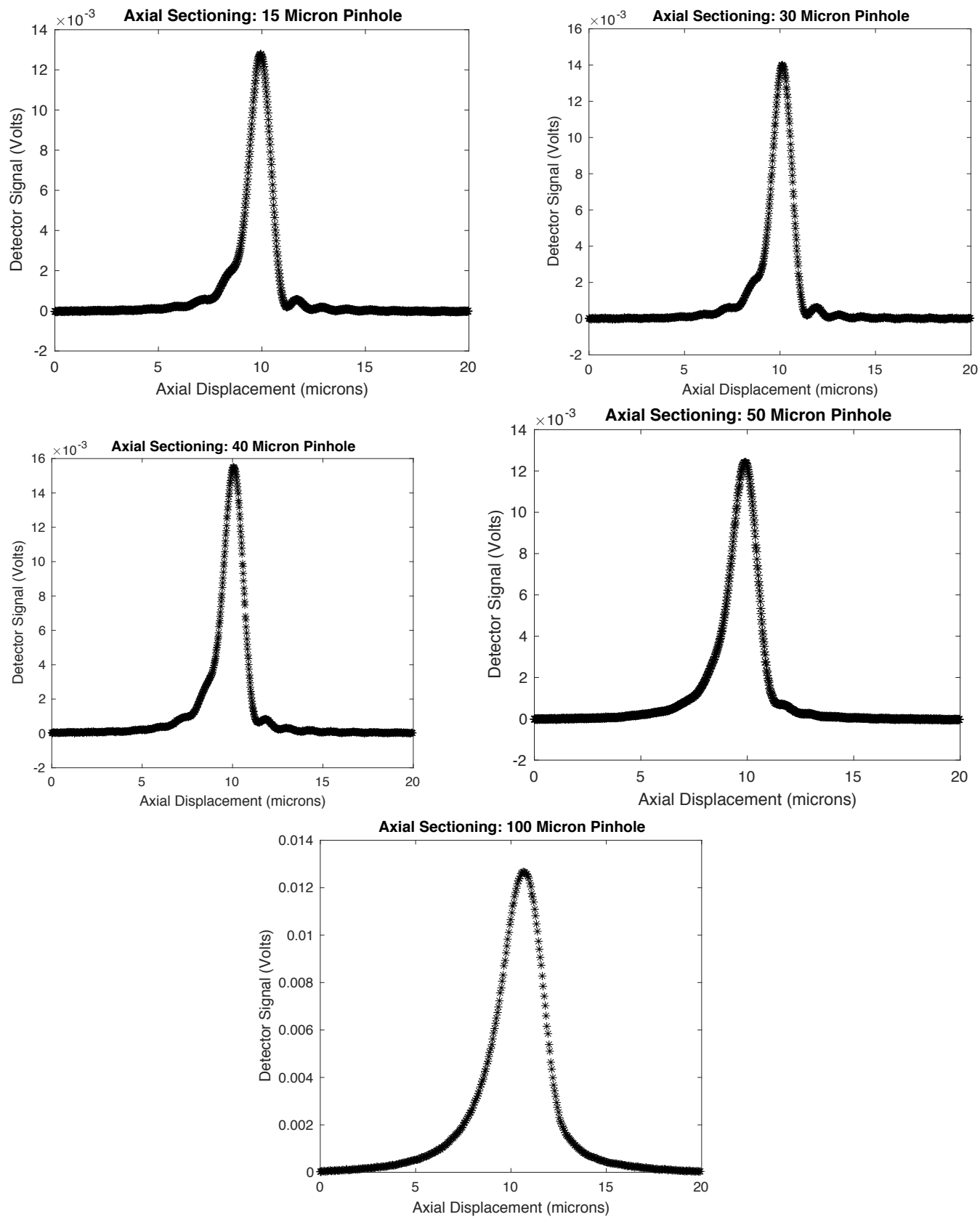


Figure 23: Axial Sectioning Data for 15, 30, 40, 50, and 100 μm Pinholes.

Pinhole Diameter Size (μm)	Theoretical FWHM	Experimental FWHM	Percent Difference %
15	1.24	$1.20 \pm 7.7\%$ (n=3)	-3.2%
30	1.26	$1.18 \pm 0.36\%$ (n=3)	-6.3%
40	1.33	$1.31 \pm 1.9\%$ (n=3)	-1.5%
50	1.48	$1.39 \pm 2.6\%$ (n=3)	-6.1%
100	2.62	$2.54 \pm 1.8\%$ (n=3)	-3.1%

Table 7: Theoretical FWHM vs. Experimental FWHM for 15, 30, 40, 50, 100 μm Pinholes

This microscope performed as predicted by the Wilson and Carlini theory and due to time constraints I did not test another objective lens. Setup III was the final design used for characterization of the microscope. The next section discusses the data I collected for the axial sectioning and my assessment of the microscope.

4. Data and Analysis

To characterize the microscope, I did not return to using the milk and water mixtures as the optical phantom. Instead, I used another optical phantom created at the Center for Functional Nanomaterials (CFN) at Brookhaven National Laboratory in Upton, NY. Polydimethylsiloxane, a plastic-like material, (PDMS) and the scattering material Min-U-Sil40 were spun together onto glass slides to make the samples. PDMS is a silicon-based organic polymer [41]. This optical phantom is more similar to the structure of human tissue than the milk mixtures. Min-U-Sil40 is made up of fine ground silica beads, which range from 10.5 to 40 μm in diameter. These beads make the optical phantom have scattering properties similar to human tissue because the bead mixture mimics refractive elements in tissue, like cell bodies and subcellular organelles [21]. I worked with two sets of optical phantoms with different concentrations. The first set had

a low effective scattering coefficient and varied in thickness. The second set had higher effective scattering coefficients and also varied in thickness. I aimed to mimic the scattering properties of human skin. In a biological review done at Oregon Health Science University, scientists determined the range of μ 's for human skin to be around 30 to 70 cm^{-1} . The μ for the Dermis and Epidermis specimen was measured 45.3 and 68.7 cm^{-1} respectively [40]. By working with these two sets, I aimed to have an optical phantom within the range for human skin and to determine how variation in the effective scattering coefficient and thickness each respectively affected the axial sectioning.

4.1 Set One: Low Effective Scattering Coefficient

4.1.1 Determining Effective Scattering Coefficient

In the first set, all of the samples had the same concentration, 0.0097 mg/mL (Min-U-Sil40 to PDMS), but had different thicknesses: 200, 260, 280, and 380 μm . The effective scattering coefficient was measured using the same method and apparatus as described in Section 3.2.2. I measured the initial intensity of the beam, I_0 , and then the intensity of the beam after traveling through each sample, I . Recall the Beer-Lambert Law from Section 2.3.1,

$$I(z) = I_0 e^{-\mu z},$$

which can also be rearranged as,

$$-\mu = \frac{\ln\left(\frac{I}{I_0}\right)}{z}.$$

This law states that as thickness, z , increases, the natural log of the final to initial intensity decreases. Consequently since I_0 is a constant, the natural log of the intensity ratio decreases when I decreases. Using the Beer-Lambert Law, I anticipated as the thickness increased, the beam would be less intense. The data displayed exactly this

because more light was lost traveling through the thicker samples. The results are in

Table 8.

z	I_0	I	$\ln(I/I_0)$
200	562	550	-0.021583572
260	562	545	-0.030716055
280	562	543	-0.03439253
380	562	535	-0.049235103

Table 8: Effective Scattering Coefficient Measurements for Samples with Thicknesses: 200, 260, 280, and 380 μm . This table shows the measurements, where z is the thickness of the sample in μm , I_0 is the initial beam intensity in millivolts, and I is the beam intensity after the sample in millivolts. This table was made using Microsoft Excel.

As seen in the table, there was not a significant amount of light lost because the samples had a low concentration. Using the Beer-Lambert Law, I graphed $\ln(I/I_0)$ vs. z to calculate the effective scattering coefficient. Figure 24 displays the graph.

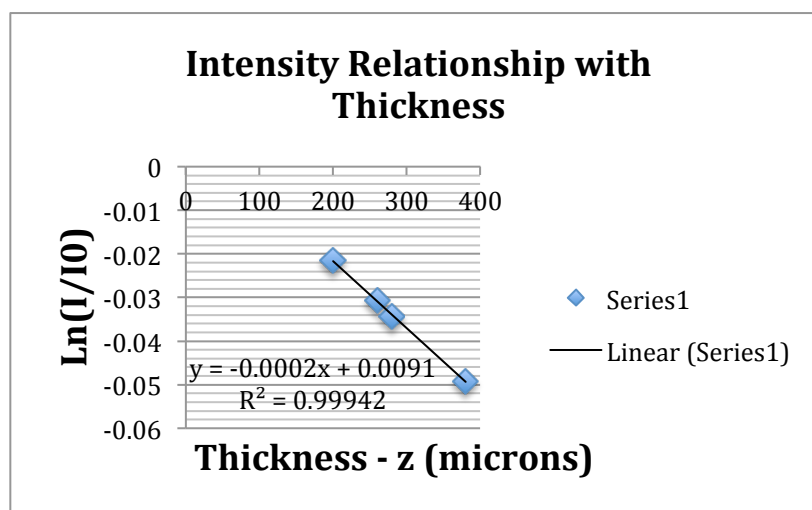


Figure 24: Intensity Relationship with Thickness for Samples 200, 260, 280, and 380 μm Thick. The absolute value of the slope of the line is the effective scattering coefficient. The thickness and natural log of the final and initial intensity have an inverse variation relationship. As the thickness increases, the natural log of intensity decreases linearly.

The effective scattering coefficient of the optical phantom was 2 cm^{-1} . This optical phantom was lower than my targeted range, 30 to 70 cm^{-1} . However, a live sample with a similar coefficient to the optical phantom is soft tissue of the lung, which has a scattering

coefficient of 8.1 cm^{-1} [40]. After I took this measurement, I proceeded to examine how different thicknesses of this optical phantom affected the axial sectioning.

4.1.2 Axial Sectioning Results and Analysis

Before I imaged the optical phantom samples, I imaged the mirror without a sample for reference. All data was taken using the $50\mu\text{m}$ pinhole. The theoretical axial sectioning with air is $1.48\mu\text{m}$. The experimental axial sectioning was $1.32 \pm 2.2\%$. (This difference in axial sectioning was most likely caused by shifts in the microscope.

Alignment was extremely difficult with this system. Data taken on different days had slight variations, which is one of the reasons why it is so difficult to standardize these microscopes with their inconsistencies.) I began to image the optical phantom samples.

There were two ways to mount the samples. They had glass on one side and the scattering material on the other. The scattering material side was slightly curved (exaggerated in the figure) because of how they were constructed with the spinner. The two possible orientations are displayed in Figure 25.

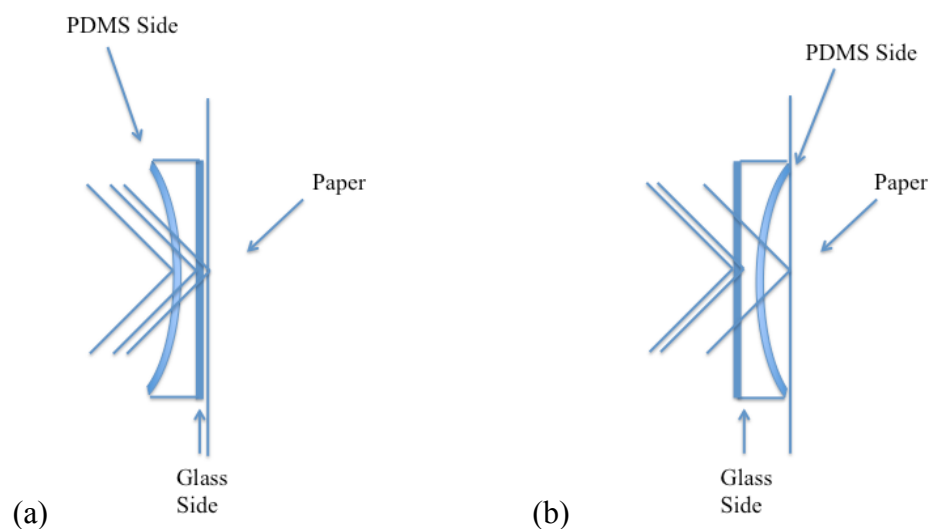


Figure 25: (a) Optical Phantom Sample Mounted with Scattering Material Facing the Objective Lens. The first reflection is off of the PDMS surface. The second is off the glass and the third is off the paper. (b) Optical Phantom Sample Mounted with the Glass

Facing the Objective Lens. The first reflection is off the first surface of the glass and the second is the second surface of the glass. The third is off the paper.

I taped the corners of the sample to a white piece of paper. The paper was then attached to a flat mounting with double-sided tape. I mounted the $200\mu\text{m}$ sample with the PDMS side facing the objective lens. By adjusting the axial position of the sample, I imaged the three surfaces by bringing them each into the focal plane. Figure 26 shows the axial sectioning graphs for when the three surfaces were in the focal plane.

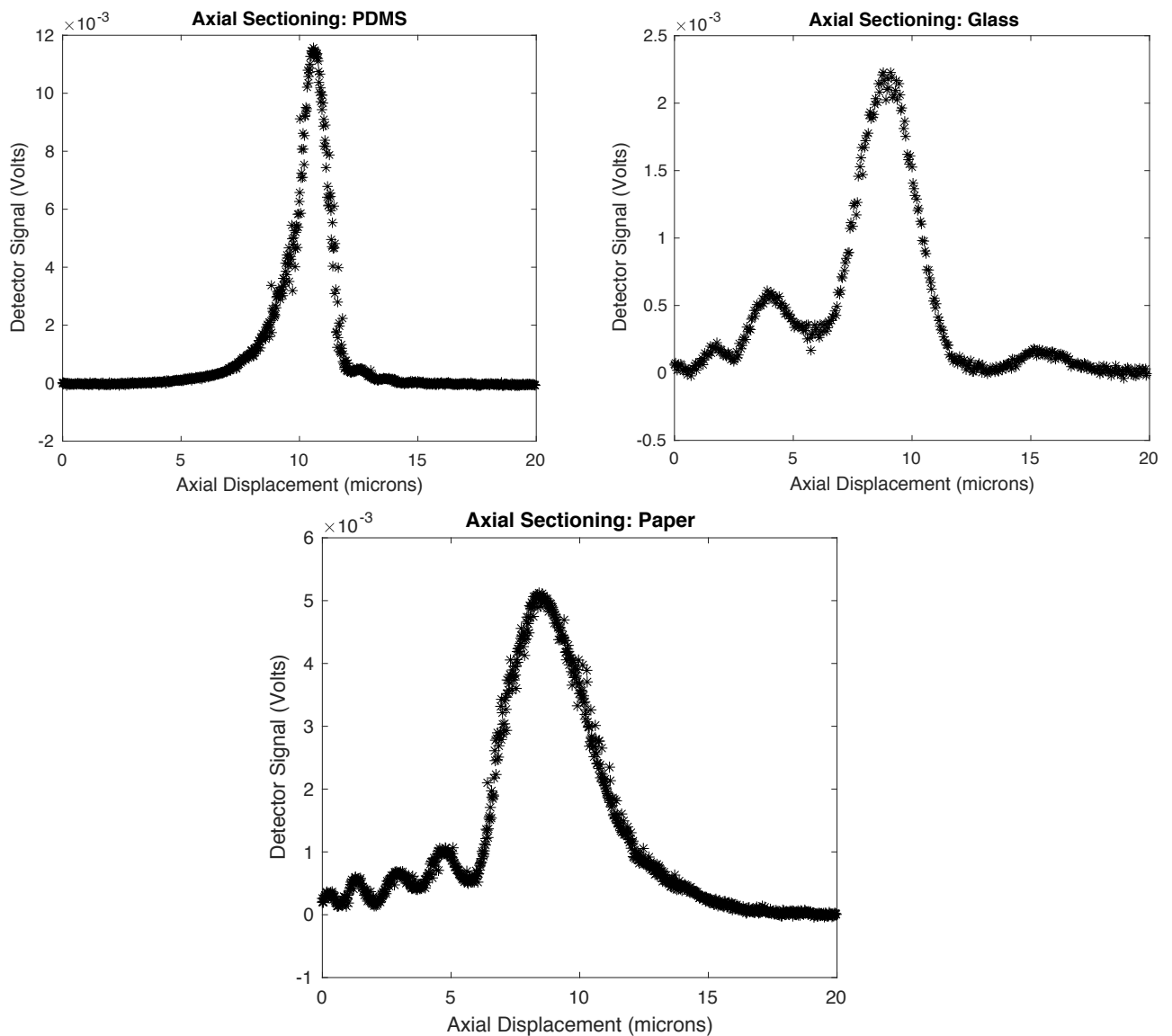
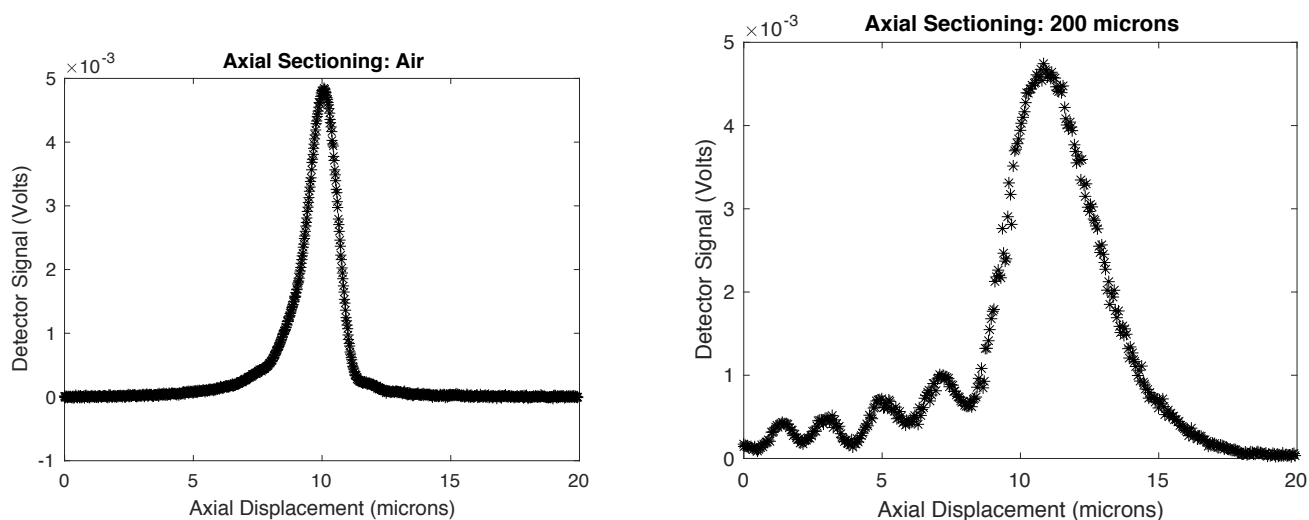


Figure 26: Axial Sectioning Data Graphs for the PDMS, Glass and Paper at the Focal Plane. To change which surface the beam reflects off of, the axial distance, the distance

between the sample and objective lens, is adjusted. The first interface is Air-PDMS, where the PDMS is in the focal plane; then the PDMS-Glass interface, where the glass is in the focal plane; and lastly the Glass-Paper interface, where the paper is in the focal plane. When the beam reflects off of the first interface, Air-PDMS, the sample is farther from the objective lens. When the beam reflects off of the last interface, Glass-Paper, the sample is closer to the objective lens.

The axial sectioning of the graphs were 1.44, 2.98, and $3.95\mu\text{m}$ for PDMS, glass, and paper at the focal plane respectively. The FWHM of the glass graph was the thinnest because the beam did not travel through any scattering media. Accordingly, this width was close to the predicted FWHM for imaging through air with just the mirror. In the axial sectioning graphs, where the focus was at the glass and paper, spherical aberrations started to appear. The FWHM got larger in both graphs because the beam was traveling through the scattering material. The intensity of the beam also decreased because more light was lost to scattering. Through this investigation, I learned to distinguish between the different peaks and made sure the paper was in the focal plane to image through the entire sample.

The axial sectioning graphs for this set are shown in Figure 27. I predicted that the thicker samples would yield a wider FWHM. However, the opposite in fact occurred.



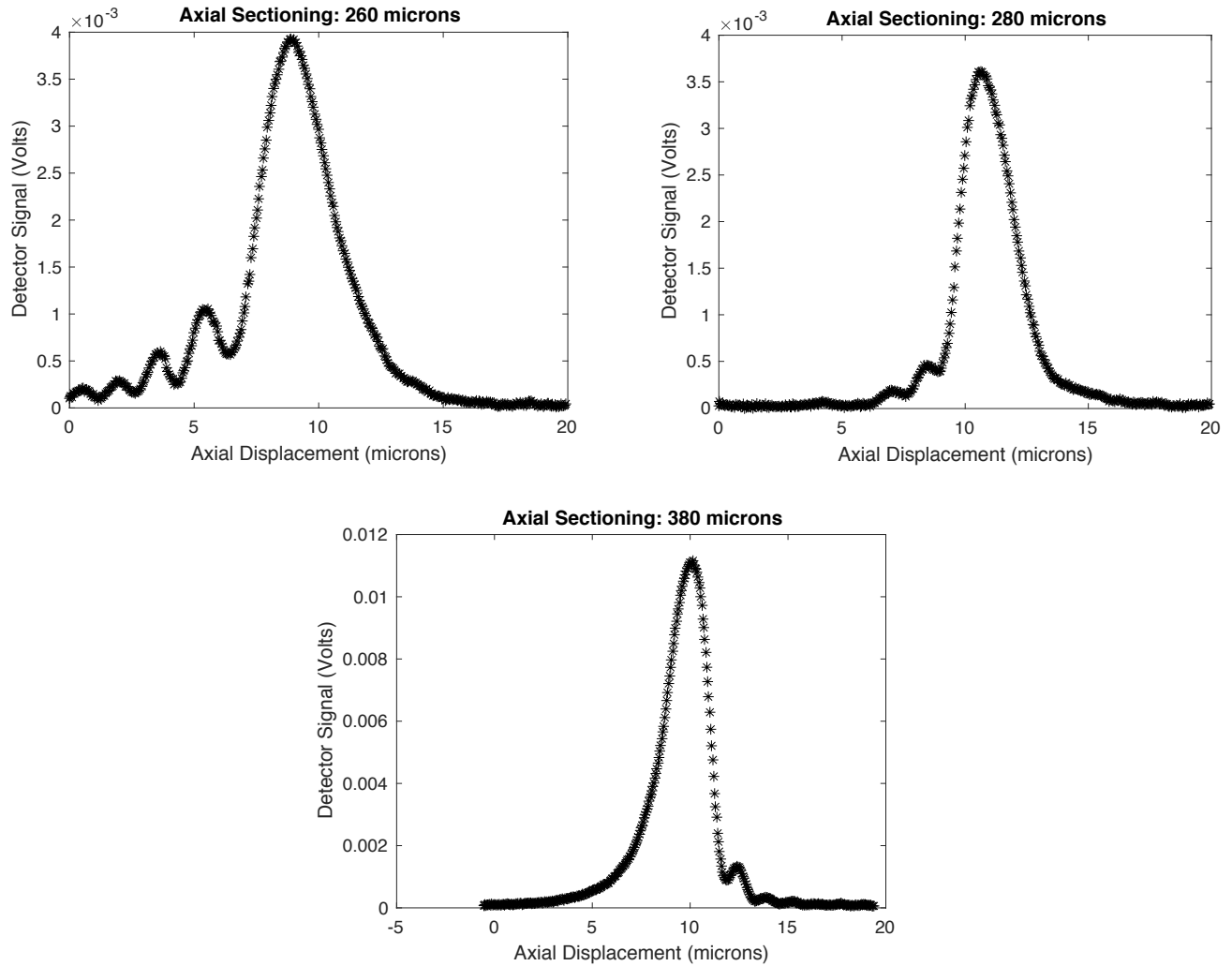


Figure 27: Axial Sectioning Data Graphs for Air, and Samples 200, 260, 280, and 380 μm .

The axial sectioning of the graphs were $1.32 \pm 1.7\%$, $3.58 \pm 9.9\%$, $3.12 \pm 5.2\%$, $2.34 \pm 1.3\%$, and $2.47 \pm 1.1\%$ μm ($n=3$) for the air, the 200, 260, 280, and 380 μm samples respectively.

As the thickness increased, the FWHM did not follow a particular pattern.

This revealed that another variable was influencing the axial sectioning, other than the change in thickness. Further evidence of an additional variable at work was the spherical aberrations present in the graphs. I concluded that these spherical aberrations indicated a change in the refractive index. Because of the technique used to mount the samples, an

air gap was introduced between the sample and the paper. I only used tape to attach the sample and if the sample was not fully in contact with the paper, the beam would travel from a refractive index 1.4 for PDMS to a refractive index 1.0 for the air. This explains the spherical aberrations present in the graphs. This mismatch in refractive index led to the light focusing at different points, resulting in multiple peaks in the graphs. Also, the 280 and 380 microns graphs did not experience a lot of spherical aberrations. Their FWHMs did not get larger as the thickness increased. This led me to conclude that the scattering coefficient was too low and the variation in thickness did not have any effect on the axial sectioning.

It is evident in the axial response graph in Figure 28 that another variable was affecting the axial sectioning, besides the effective scattering coefficient. The signals were calculated by $10\log_{10}(I/I_{\max})$.

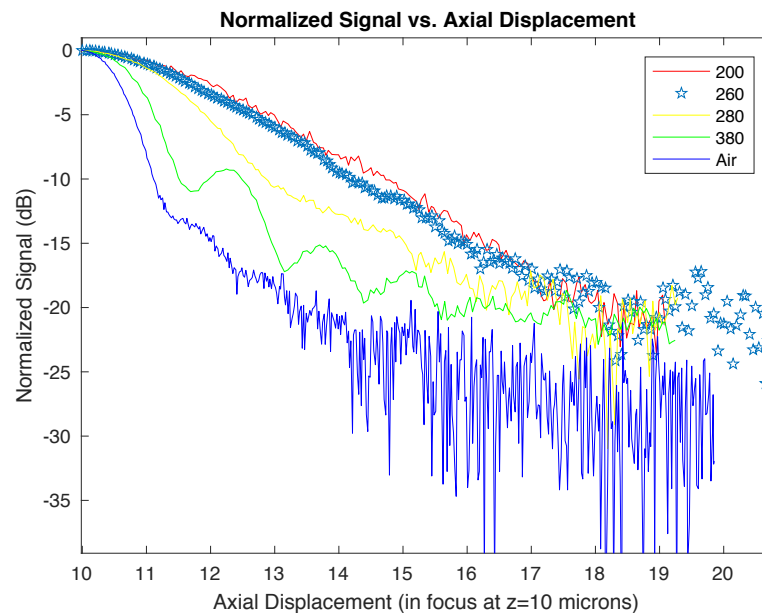


Figure 28: Axial Response Graph. This is the axial response of the microscope when imaging through the four samples, 200, 260, 280, and 380 μm thick, compared with air.

If the effective scattering coefficient was the only variable changing the axial sectioning, then the thinnest sample, 200 μm , should have had the least degradation in resolution compared to the other three samples. However, the thickest sample, 380 μm , had the best resolution. This data showed the opposite of the original hypothesis because more factors were at work than originally anticipated.

This first set of optical phantoms showed that with a low scattering coefficient, the variation in thickness does not affect the axial sectioning. The low scattering coefficient becomes overwhelmed by other variables, like spherical aberrations in this case. This data also illuminated the fact that I needed to change the method of mounting the samples and not introduce a mismatch in refractive index. This led me to explore higher concentrations of the PDMS with Min-U-Sil40.

4.2 Set Two: High Effective Scattering Coefficient

4.2.1 Determining Effective Scattering Coefficients

The second set consisted of three samples that varied in concentration and thickness. Because of this variation, I could not calculate the effective scattering coefficient with a linear plot as before. Instead, I used equation (13) from Section 2.3.1:

$$I(z) = I_0 e^{-\mu z}.$$

Then, I solved the equation for μ , the effective scattering coefficient:

$$\mu = -\frac{\ln\left(\frac{I}{I_0}\right)}{z}.$$

I measured the voltage of the initial beam and the voltage of the beam after it went through the sample. Using a digital micrometer, I measured the thickness of each sample. With this information, I solved the equation for the effective scattering coefficient. With these samples, μ varied spatially, so I took measurements of four different spots on the

sample. Table 9 displays the data I collected for each sample. The each sample had a range of μ 's, illustrated in Table 10.

Sample	z (microns)	μ (cm^{-1})
A	400	$118 \pm 15\%$ ($n=4$)
B	210	$116 \pm 20\%$ ($n=4$)
C	270	$35.3 \pm 23\%$ ($n=4$)

Table 9: Effective Scattering Coefficient Data for Samples A, B, and C. Samples A and B had approximately the same μ . Sample C had a lower μ . All samples varied in thickness.

Samples	A	B	C
Trial 1	113	104	29
Trial 2	103	112	47
Trial 3	144	97	30
Trial 4	110	150	34

Table 10: Range of μ 's (cm^{-1}) for Samples A, B, and C. Each sample had a range of μ 's because of the surface variation.

Sample A had a concentration of 0.24 mg/mL (Min-U-Sil40 to PDMS) and was spun at 1000 revolutions per minute (RPM) for 30 seconds. Sample B had the same concentration as Sample A, 0.24 mg/mL, but was spun at 3000 RPM for 30 seconds. Lastly, Sample C had a concentration of 0.024mg/mL and was spun at 2000 RPM for 30 seconds. Among the three, Sample A had the highest effective scattering coefficient, followed by B and C. This verified that Sample A and B had the same concentration because their effective scattering coefficients were approximately the equal. These samples were closer to the range for human skin. Sample C was actually within the range and Samples A and B were just above it. Compared to actual biological sample, Samples A and B had a μ closest to the Epidermis specimen, 68.7 cm^{-1} [40]. The effective scattering coefficient varied within each sample.

4.2.2 Measuring Thickness

I measured the thickness of the samples with a micrometer, but I wanted to compare how the spin rate of the samples matched their thicknesses. Ideally, the relationship between spin speed and the thickness of the samples should roughly follow:

$$t \propto \frac{1}{\sqrt{\omega}} \quad (17),$$

where t is the thickness of the sample and ω is the angular velocity or spin rate. The thickness of the film is also influenced by the concentration [42]. Figure 29(a) shows the relationship I observed between the spin rate and the thickness for each sample. I confirmed the relationship between the thickness and spin rate by taking the log of both sides of Eq. 17:

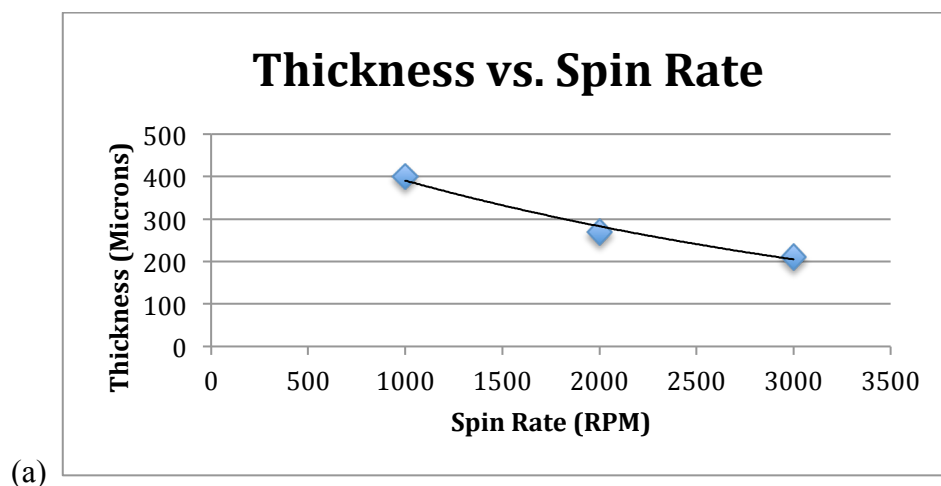
$$\log(t) \propto \log\left(\frac{1}{\sqrt{\omega}}\right).$$

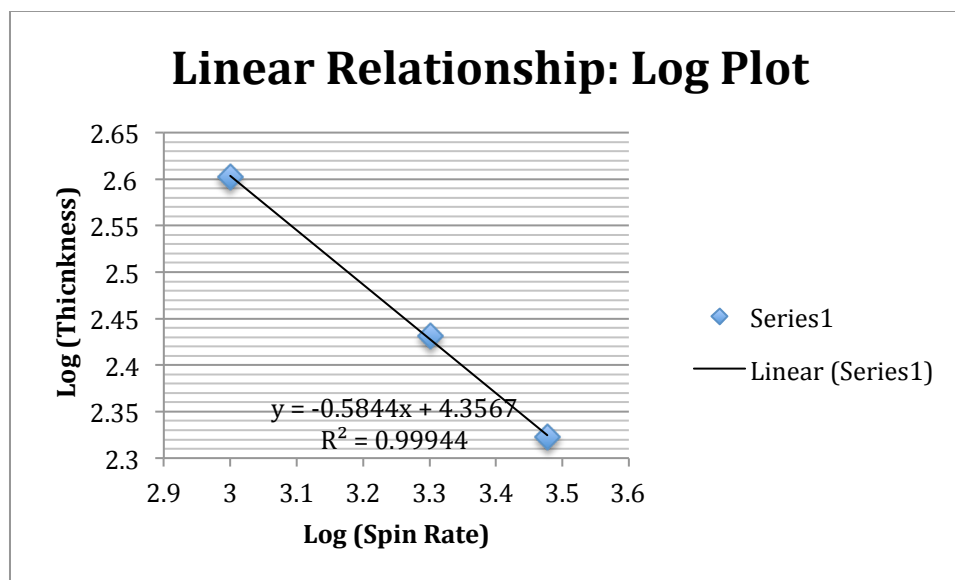
Then I rewrote it as:

$$\log(t) \propto -\frac{1}{2} \log(\omega). \quad (18)$$

The relationship between $\log(t)$ and $\log(\omega)$ is a line with the slope of negative one half.

Figure 29(b) illustrates that the samples followed the relationship of Eq. 18.





(b)

Figure 29: Thickness and Spin Rate. (a) Thickness vs. Spin Rate Graph. This shows the exponential decay relationship between the thickness and the spin rate. (b) Log Plot: Log (Thickness) vs. Log (Spin Rate). This shows the linear relationship between the log of thickness and the log of spin rate. The slope is approximately the correct value of negative one half.

The spin rate and thickness relationship roughly follows an exponential decay curve as expected. The slower the samples are spun, the thicker they are. As the spin rate increases, the thickness decreases in an exponential decay. The samples matched Eq. 18 because the slope is around negative one half for the linear relationship. After I confirmed that the properties of each sample matched the data, I began to image the optical phantoms with the microscope.

4.2.3 Axial Sectioning Results and Analysis

I started imaging the mirror without a sample for reference. I took the data with the $50\mu\text{m}$ pinhole. With this second set, I mounted the samples on the mirror with the glass side facing the objective lens. I set the corrective collar on the objective lens to .170 mm to account for the thickness of the glass. To prevent an air gap from occurring between the sample and the mirror, I put a small drop of oil on the mirror and placed the

sample on top. The oil has a refractive index 1.518 and PDMS has a refractive index 1.4; this difference is not as drastic as the PDMS to air.

The microscope's alignment shifted a bit since I first compared it to the Wilson and Carlini theory. Despite attempts to adjust it back to its original position, I could not perfectly match the experimental FWHM with the theoretical FWHM, but it was accurate enough. This data served as the baseline for comparison. Table 11 shows the data for axial sectioning.

Sample	μ (cm^{-1})	Reference Air FWHM (n=3) (μm)	Optical Phantom FWHM (n=3) (μm)	Percent increase %
A	$118 \pm 15\%$ (n=4)	$1.931 \pm 0.7\%$	$3.941 \pm 6.4\%$	104.1%
B	$116 \pm 20\%$ (n=4)	$2.040 \pm 1.6\%$	$2.430 \pm 1.9\%$	19.1%
C	$35.3 \pm 23\%$ (n=4)	$1.751 \pm 2.7\%$	$3.535 \pm 3.9\%$	101.9%

Table 11: Axial Sectioning Data for Samples A, B, C with 50 μm Pinhole. Note: For these trials, I imaged through the same spot on the sample.

When imaging through the optical phantoms, the FWHM for all three samples increased compared to the reference as predicted. Looking at Samples A and B, which have the same concentration, it seemed that at first glance the difference in thickness caused a drastic increase in the FWHM. For Sample A, the thicker sample, the FWHM increased by over 100%, but for Sample B, the thinner sample, the FWHM only increased by 19%. I expected the thicker sample to have a larger FWHM, yet after seeing this data, I suspected more than the thickness was affecting the FWHM because of the severity of the increase. The additional factor I did not take into account was the variations in the samples themselves (I realized sample variation after I took these measurements and then I measured the μ 's); the Min-U-Sil40 was not spread out uniformly. Some parts of the

samples had more scattering material than others. Also, the surfaces of the samples were inconsistent; they had bumps and ripples, which would affect the FWHM.

For Sample C, the axial sectioning changed immensely too. This sample had a lower scattering coefficient and had a thickness in between Samples A and B. Yet, this high percent increase did not match with its effective scattering coefficient. It had a lower coefficient than Sample A and was thinner, and yet its FWHM increased by approximately the same amount as Sample A. But then again, these samples were not as consistent as I planned. Depending on the spot of the sample the microscope was imaging through, this axial sectioning would be completely different.

For all of the samples, the FWHM increased compared to the reference FWHM. This is shown more clearly in Figure 30.

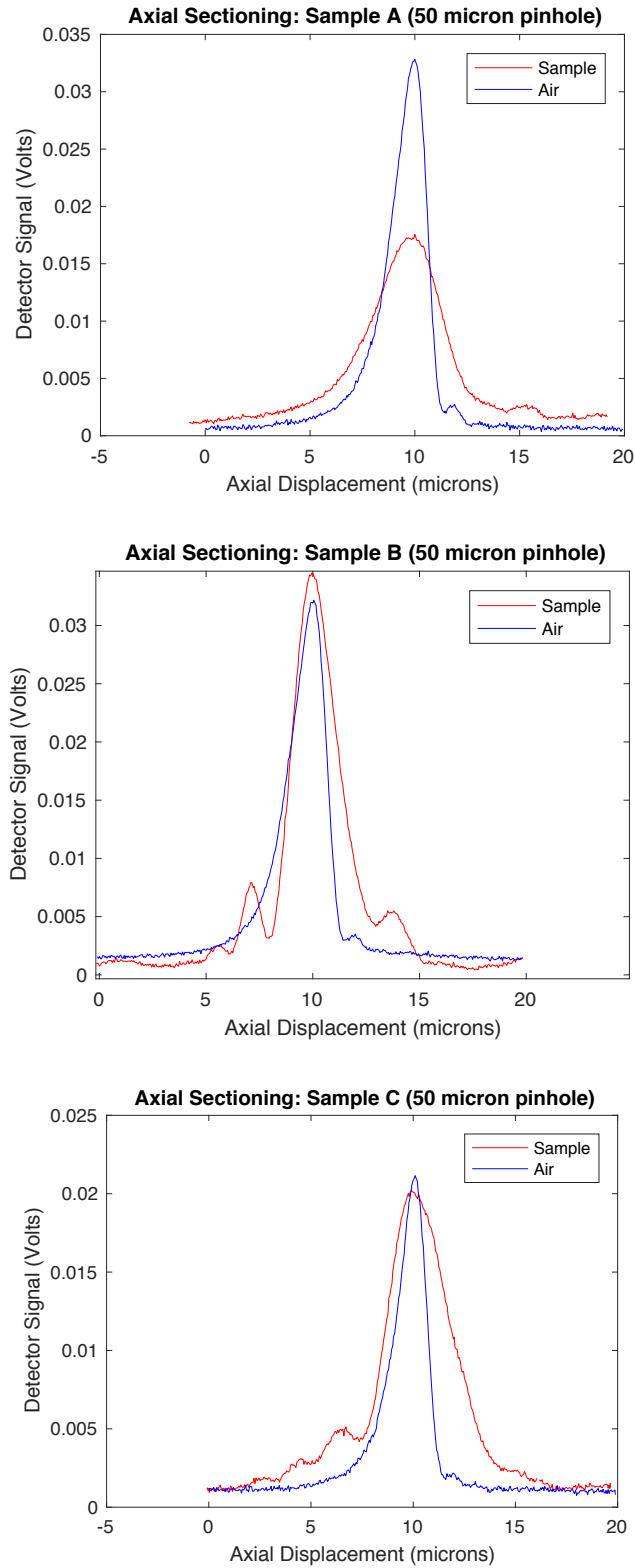
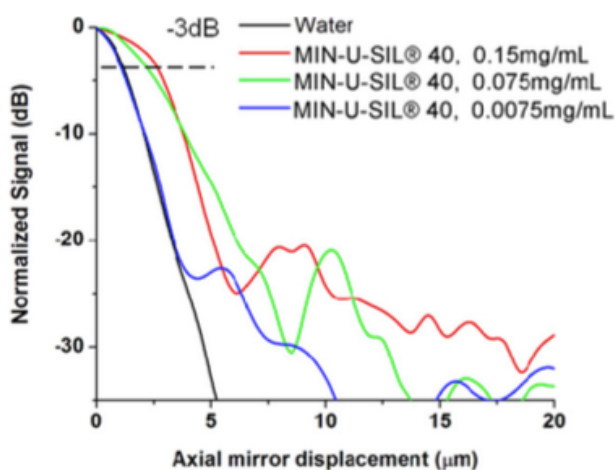


Figure 30: Axial Sectioning Comparison Graphs for Samples A, B, and C with $50\mu\text{m}$ pinhole. The blue curves represent the axial sectioning when imaged through air, the

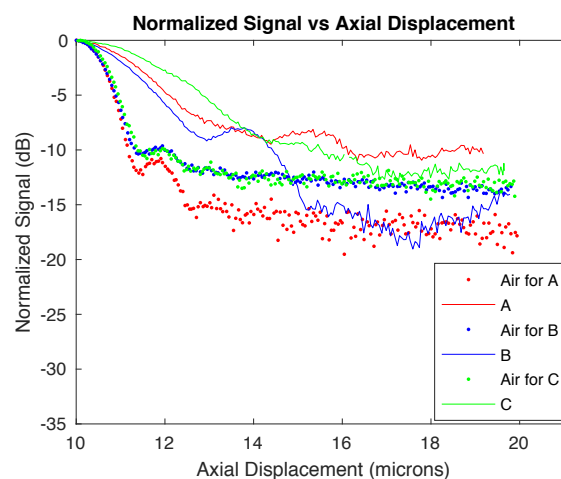
reference data. The red curves represent the axial sectioning when imaged through the optical phantom sample.

As seen in the three graphs above, when the microscope imaged through a medium with scattering material, the FWHM increased. The revised mounting technique with the oil greatly reduced the spherical aberrations. The detector signal varied, but typically decreased because more light was lost due to scattering.

In the study done at Stony Brook University, Danni Wang et al. also used Min-U-Sil40 in their optical phantoms. Similar to my experiment, they tested different concentrations of the Min-U-Sil40 with water to determine the one that yielded most stable and reproducible results. Their data is shown in Figure 31(a). They found that concentrations in the range of 0.0075 mg/mL to 0.075 mg/mL were the most reliable. To compare my data with Stony Brook's, the axial response graph for the three samples is displayed in Figure 31(b).



(a)



(b)

Figure 31: (a) “The axial response of the DAC microscope when investigating different concentrations of Min-U-Sil40 bead suspension.” D. Wang, Y. Chen, and J.T.C. Liu, *Biomedical Optics Express* Biomed. Opt. Express 3, 3153 (2012). (b) Axial Response Graph for Samples A, B, and C.

Note in the Stony Brook data their focus was at $0 \mu\text{m}$, while in my experiment, it was at $10 \mu\text{m}$. Also, the Stony Brook samples had the one reference imaged through water, but my samples had their respective references imaged through air. Sample A experienced the most signal degradation, followed by C and B. Table 12 gives a more detailed comparison of my data to the Stony Brook data.

Sample	μ (cm^{-1})	Thickness (μm)	Reference FWHM (μm)	Optical Phantom FWHM (μm)	Percent Increase %
0.15 mg/mL Min-U-Sil40 to Water	773 (n=1) (<i>unstable</i>)	~100	$2.1 \pm 5\%$	3.1	47.6%
0.075 mg/mL Min-U-Sil40 to Water	$118 \pm 18\%$ (n=6)	~100	$2.1 \pm 5\%$	$3.7 \pm 26\%$	76.2%
0.0075 mg/mL Min-U-Sil40 to Water	$19 \pm 16\%$ (n=6)	~100	$2.1 \pm 5\%$	$2.2 \pm 10\%$	4.76%
A (0.24 mg/mL Min-U-Sil40 to PDMS)	$118 \pm 15\%$ (n=4)	400	$1.931 \pm 0.7\%$ (n=3)	$3.941 \pm 6.4\%$ (n=3)	104.1%
B (0.24 mg/mL Min-U-Sil40 to PDMS)	$116 \pm 20\%$ (n=4)	210	$2.040 \pm 1.6\%$ (n=3)	$2.430 \pm 1.9\%$ (n=3)	19.1%
C (0.024 mg/mL Min-U-Sil40 to PDMS)	$35.3 \pm 23\%$ (n=4)	270	$1.751 \pm 2.7\%$ (n=3)	$3.535 \pm 3.9\%$ (n=3)	101.9%

Table 12: Comparison of Stony Brook Data to My Data. D. Wang, Y. Chen, and J.T.C. Liu, Biomedical Optics Express Biomed. Opt. Express 3, 3153 (2012). Note: For the trials in my data, I imaged through the same spot on the sample.

In the Stony Brook data, as the effective scattering coefficient increased, the axial sectioning increased. This was also true for my data. The axial sectioning for Samples A and C increased more than 100%, which is high compared to the percent increases for the Stony Brook samples, which did not exceed 76%. The optical phantoms I used also had

PDMS with Min-U-Sil40, while the Stony Brook phantoms were Min-U-Sil40 with water. However, the effective scattering coefficients for all the samples were relatively within the same range, so that could not be the cause of this difference. The samples did differ in thickness though; Samples A, B, C were a lot thicker. This might indicate that as the thickness increases the FWHM increases as well, but more data is needed to confirm this. The statistics for the Min-U-Sil40 with water samples were better than the PDMS with Min-U-Sil40 ones because more trials were run. Due to time limitations, I was only able to perform three trials.

A crucial misstep in my data collection was I did not move the sample around while imaging. I ran four trials imaging through the same spot for each sample. I realized afterwards I did not consider the variations in the samples themselves. From my data, I can conclude that as the scattering coefficient increased the FWHM did as well. With the higher scattering coefficient, variation in thickness affected the axial sectioning. This indicates I am on the right track, yet more data needs to be collected to specifically identify the relationship of how variation in μ affects the axial sectioning. I attempted to handle too many variables at once and need to focus on one at a time in the future. An additional fantastic conclusion is the samples proved to be a great mixture for the optical phantom. They were reproducible and could be made with various thicknesses. They were solid and remained stable throughout data collection. The surface of the samples varied, which is representative of an actual sample. Although my research with the microscope is ending, I can plan how the future imaging techniques should proceed in order to avoid these unforeseen challenges that I encountered.

4.3 Future Steps and Techniques

The mixture of PDMS with Min-U-Sil40 is an excellent optical phantom to continue using for imaging. I worked with a mixture that could handle various concentrations and thicknesses. This optical phantom is stable and can be reused multiple times. The μ of each sample varies spatially; meaning due to the variation of the surface, a sample has a range of μ 's. This is more representative of actual samples because they are not uniform. I worked with a wide range of scattering coefficients, so with this mixture it is possible to attain the range of μ 's for human skin and other specimens like brain and breast tissue. Because I discovered spatial variation after I took axial sectioning measurements, I only imaged through one spot on the sample. An important technique to implement for future data collection is to move the sample around and image through different spots. Because the effective scattering coefficient varies spatially, the axial sectioning has a range for each sample as well. In future data sets, this should be taken into account.

Additionally, the focus for data collection should be more narrowed. With the optical phantoms previously used, I tried changing too many variables at one time. There should be a set of at least three samples with all of the same thickness and varying μ , and then another sample set with the same μ and varying thickness. With the results from the first set, conclusions can be drawn on how varying μ influences the axial sectioning. The results from the second set should illustrate how thickness affects the axial sectioning. Samples A and B from the high scattering coefficient set had the same scattering coefficient, but had different thicknesses as well. I only had one sample, C, with a different scattering coefficient and a different thickness. Because of many variables

among the three samples, it was impossible to clearly distinguish the effect μ and thickness had on axial sectioning. If there is a group of samples, where only one variable changes at a time, then the direct relationship can be clearly seen.

Another principal technique of data collection is to take numerous trials. Because of time limitations, I could not afford to run as many trials as I would have liked. The greater number of trials allows for a better spread of data. Like the data recorded at Stony Brook, I think the optimal number of trials to take is at least six. Six trials would have better statistics than the data I was able to take with three trials per sample. If time permitted, taking more trials is an improvement. With a better spread and statistics, the data would be more revealing of the how exactly μ affects the axial sectioning. My data did not have a large spread and this definitely contributed to the vague relationship I observed. Increasing the number of trials in the future would greatly enhance the data.

From my research, I learned useful lessons relevant for applications for future imaging. The apparatus and method I created to measure the effective scattering coefficient of an optical phantom is a reliable and logical way to do so. It worked smoothly throughout my data collection and would be a smart technique to use in the upcoming data sets. I also learned when examining the relationship between thickness and axial sectioning, the concentration of the optical phantom should be higher than 0.0097 mg/mL. I found that with a lower scattering coefficient, the relationship is not evident because it is susceptible to influences of other factors, like spherical aberrations. A side investigation can be done to determine the lowest concentration when the variation in thickness starts to impact the axial sectioning. Lastly, I discovered the orientation of mounting the sample is significant. To prevent from inadvertently

introducing a mismatch in refractive index, the best way to mount the sample is with the glass side facing the objective lens, adjust the corrective collar on the objective lens to account for the thickness of the glass, and put a drop of oil between the sample and the mirror. This solved my problem with spherical aberrations. By incorporating these lessons, some of the challenges I experienced can be avoided.

Once the relationships between μ and axial sectioning, and thickness and axial sectioning are found, the purpose of this study is achieved. However, the long-term goal of this project is to image live samples. To work towards this goal, the set-up of the microscope would have to be adjusted to include the scanners once more. I removed them because I was having trouble with alignment. Challenges still lie ahead with alignment and getting the system to function properly with the new set up. Although the possibility to image actual samples is far into the future, this goal is quite attainable with more research and time.

4.4 Pilot Study

This section includes more data that I collected, but was unable to make any concrete conclusions about. However, it may be of interest to future researchers. I was interested in how the change in pinhole size affects the axial sectioning when imaging the optical phantoms. The theory of Wilson and Carlini explains that as the pinhole size increases, the FWHM increases. At the start, I proved that the microscope was functioning properly and followed this theory, but how does it behave when imaging the optical phantoms? This was the question I wished to address. I switched the pinhole from the 50 μm to the 100 μm pinhole. Table 13 shows the data with the 100 μm pinhole

compared to the data with the 50 μm pinhole. The theoretical FWHM for the reference graph, according to Wilson and Carlini, is 2.62 μm .

Samples	A	B	C
Thickness (μm)	400	210	270
μ (cm^{-1})	$118 \pm 15\%$ (n=4)	$116 \pm 20\%$ (n=4)	$35.3 \pm 23\%$ (n=4)
Reference Air FWHM with 100 μm (n=3) (μm)	$2.80 \pm 2.5\%$	$2.73 \pm 0.91\%$	$2.94 \pm 2.5\%$
Optical Phantom FWHM with 100 μm (n=3) (μm)	$5.97 \pm 4.5\%$	$3.12 \pm 8.5\%$	$4.31 \pm 5.3\%$
Percent increase % with 100 μm	113.2%	14.3%	46.6%
Reference Air FWHM with 50 μm (n=3) (μm)	$1.931 \pm 0.7\%$	$2.040 \pm 1.6\%$	$1.751 \pm 2.7\%$
Optical Phantom FWHM with 50 μm (n=3) (μm)	$3.941 \pm 6.4\%$	$2.430 \pm 1.9\%$	$3.535 \pm 3.9\%$
Percent increase % 50 μm	104.1%	19.1%	101.9%

Table 13: Axial Sectioning Data for Samples A, B, C with 100 μm Pinhole. The last two columns compare the percent increase of the 100 μm to the 50 μm pinhole.

Compared to the 50 μm pinhole data, the FWHM increases only for sample A with the 100 μm pinhole. For the other two samples, the 100 μm data did not follow the same pattern as the 50 μm data. There was not an increase in FWHM, when the pinhole increased. These samples had both thickness and μ changing at once. I added an additional variable, the pinhole size. Figure 32 displays the axial sectioning graphs for the

data with the 100 μm pinhole. The graphs compare the axial sectioning of the samples to the reference axial sectioning. In all of the graphs, the axial sectioning increased, which indicates a step in the right direction. However because of all the variables, I am unable to make any observations on how exactly the change in pinhole size affects the axial sectioning. Sample sets where a single variable is adjusted at a time need to be used to narrow down this correlation. Therefore, more investigation into this matter is required.

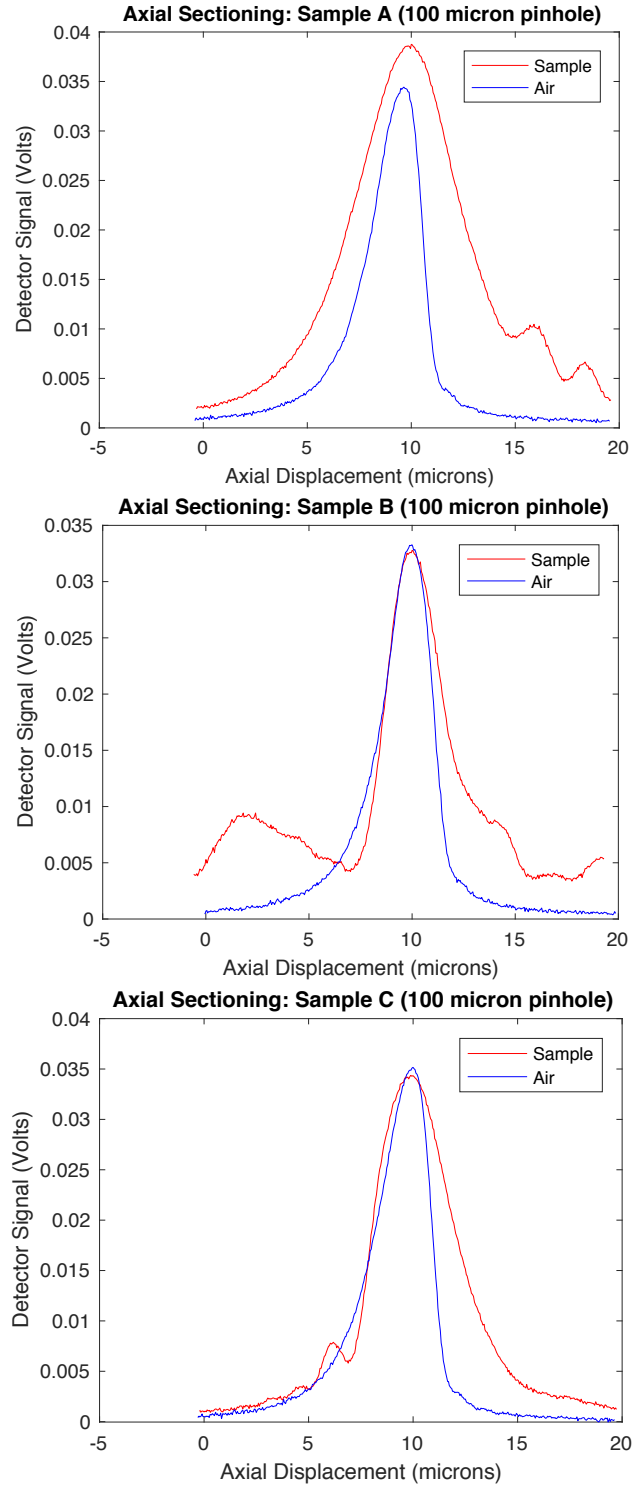


Figure 32: Axial Sectioning Comparison Graphs for Samples A, B, and C With the 100 μm pinhole. The blue curves represent the axial sectioning when imaged through air. The red curves represent the axial sectioning when imaged through the optical phantom sample.

5. Conclusion

My research originated from the interest in imaging human tissue with a confocal microscope. The confocal microscope has made its mark in clinical studies of point-of-care pathology, where patients are able to receive rapid diagnosis of abnormalities, like skin cancer. This type of microscope is unique because it has a pinhole that blocks out all unfocused light, yielding clearer and structurally defined images. It is capable of deep optical sectioning and is known for its ability to image thick samples.

With the future goal to image an actual human sample, I constructed a reflectance scanning confocal microscope. I accomplished designing and building a functioning microscope and completed the first step towards imaging live samples: characterizing the microscope with optical phantoms. I assessed the microscope's axial sectioning with two sets of optical phantoms that varied in scattering coefficient and thickness. With the optical phantoms, I aimed to mimic human skin that has a scattering coefficient in the range 30 to 70cm⁻¹.

The microscope went through three stages of development. The final setup matched the predictions of the Wilson and Carlini theory, which proved to me the system was functioning properly. The optical phantom I used was a mixture of PDMS with Min-U-Sil40 at different concentrations. PDMS is a plastic like material and the Min-U-Sil40 is a wonderful scattering material made up of fine ground silica beads, which range from 10.5 to 40 μm in diameter. These beads make the optical phantom have scattering properties similar to human tissue. The first set of phantoms consisted of four samples and varied in thickness. All four samples had the same effective scattering coefficient, 2 cm⁻¹. From this set, I concluded that with a low scattering coefficient changes in

thickness do not affect axial sectioning. The second set of optical phantoms consisted of three samples that varied in effective scattering coefficient and thickness. Two of the samples had the same scattering coefficient, around 118 cm^{-1} , and one had a scattering coefficient of 35 cm^{-1} . I observed that with a high scattering coefficient variation in thickness does affect the axial sectioning.

More data needs to be taken to clearly identify how the scattering coefficient and thickness each affect the axial sectioning. I tried to change too many variables at once and did not account for variations in the sample when measuring the axial sectioning. For future data, this optical phantom is ideal to use because it aligns with the properties for human skin and has proven to be stable and reusable. I have completed the initial step in preparing the microscope to image biological samples. Diagnosing cancer is only one of the many possible applications for confocal microscopes. By contributing to numerous biological discoveries, confocal microscopy not only improves the practice of healthcare and human lives, but also redefines the way humans are able to examine their bodies.

References

- [1] S.W. Paddock, T.J. Fellers, and M.W. Davidson. "Introductory Confocal Concepts." *Nikon Microscopy U*.
<https://www.microscopyu.com/techniques/confocal/introductory-confocal-concepts> .
- [2] J.B. Pawley, *Handbook of Biological Confocal Microscopy* (Plenum Press, New York, 2006).
- [3] "Introduction to Confocal Microscopy." *Journal of Investigative Dermatology*. Nature Publishing Group, 2012.
<http://www.nature.com/jid/journal/v132/n12/full/jid2012429a.html>.
- [4] F.L. Pedrotti, L.M. Pedrotti, and L.S. Pedrotti, *Introduction to Optics* (Pearson Education, Harlow, 2014).
- [5] M.W. Davidson. "Numerical Aperture." *Nikon Microscopy U*.
- [6] "How Does a Confocal Microscope Work?" *How Does a Confocal Microscope Work?* <http://www.physics.emory.edu/faculty/weeks//confocal/>.
- [7] "Fluorescence." *Bio-rad*.
<https://www.bio-rad-antibodies.com/flow-cytometry-fluorescence.html>.
- [8] D. Semwogerere and E. Weeks, *Encyclopedia of Biomaterials and Biomedical Engineering*, Second Edition - Four Volume Set 705 (2008).
- [9] "Understanding Spatial Filters." *Edmund Optics*.
<https://www.edmundoptics.com/resources/application-notes/lasers/understanding-spatial-filters/>.
- [10] V. Poher, G.T. Kennedy, H.B. Manning, D.M. Owen, H.X. Zhang, E. Gu, M.D. Dawson, P.M. French, and M.A. Neil. "Improved sectioning in a slit scanning confocal microscope." *Optics letters* **33**, 1813 (2008).
- [11] W.B. Amos, J.G. White, and M. Fordham, "Characteristics of laser scanning confocal microscopes for surface texture measurements." *Appl. Opt. Applied Optics* **26**, 3239 (1987).
- [12] B. Larson, S. Abeytunge, and M. Rajadhyaksha, "Performance of full-pupil line-scanning reflectance confocal microscopy in human skin and oral mucosa *in vivo*." *Biomedical Optics Express* **2**, 2055 (2011).

- [13] J. Peatross and M. Ware, *Physics of Light and Optics* (Brigham Young University, Dept. of Physics, Provo, UT, 2011).
- [14] A.K. Dunn, C. Smithpeter, A.J. Welch, and R. Richards-Kortum, "Sources of contrast in confocal reflectance imaging." *Appl. Opt. Applied Optics* **35**, 3441 (1996).
- [15] W.R. Calhoun, H. Maeta, A. Combs, L.M. Bali, and S. Bali, "Measurement of the refractive index of highly turbid media" *Optics Letters* **35**, 1224 (2010).
- [16] T. Wilson and A.R. Carlini, "Size of the detector in confocal imaging systems," *Opt. Lett.* **12**(4), 227-229 (1987).
- [17] I.S. Saidi, S.L. Jacques, and F.K. Tittel, "Mie and Rayleigh modeling of visible-light scattering in neonatal skin." *Appl. Opt. Applied Optics* **34**, 7410 (1995).
- [18] B.W. Pogue and M.S. Patterson. "Review of tissue simulating phantoms for optical spectroscopy, imaging and dosimetry." *Opt. Journal Of Biomedical Optics* **11**, 041102 (2006).
- [19] A.L. Dayton and S.A. Prahl. "Turbid-Polyurethane Phantom for Microscopy." *Design And Performance Validation of Phantoms Used in Conjunction with Optical Measurements of Tissue* (2008).
- [20] S.L. Jacques, B. Wang, and R. Samatham. "Reflectance confocal microscopy of optical phantoms." *Biomedical Optics Express Biomed. Opt. Express* **3**, 1162 (2012).
- [21] D. Wang, Y. Chen, and J.T.C. Liu, *Biomedical Optics Express Biomed. Opt. Express* **3**, 3153 (2012).
- [22] "OBIS 660nm LX 100mW Laser" *Coherent*.
<https://www.coherent.com/lasers/laser/obis-lasers/obis-lasers>.
- [23] E. Hecht, *Optics* (Pearson, Boston, 2016).
- [24] F.M. Mims, *Getting started in electronics* (Master Publ., Niles, IL, 2014).
- [25] "Laser Diodes: How it works." *Youtube*.
https://www.youtube.com/watch?v=Dk_CbGJI41U.
- [26] T.J. Fellers and M.W. Davidson, "Laser Safety." *Nikon Microscopy U*.
<https://www.microscopyu.com/microscopy-basics/laser-safety>.

- [27] “SM05PD1A - Large Area Mounted Silicon Photodiode, 350-1100 nm, Cathode Grounded.” *Thorlabs*.
<https://www.thorlabs.com/thorproduct.cfm?partnumber=SM05PD1A>
- [28] “Si Avalanche Photodetectors.” *Thorlabs*.
https://www.thorlabs.com/newgrouppage9.cfm?objectgroup_id=6686.
- [29] “Avalanche Photodiodes.” *RP Photonics Encyclopedia*.
https://www.rp-photonics.com/avalanche_photodiodes.html.
- [30] “ADP Module C12702-12.” *Hamamatsu*.
<http://www.hamamatsu.com/us/en/C12702-12.html>
- [31] M.W. Davidson. “Numerical Aperture.” *Nikon Microscopy U*.
<https://www.microscopyu.com/microscopy-basics/numerical-aperture>.
- [32] “UCPLFLN/LUCPLFLN Objectives.” *Olympus*.
<http://www.olympuslifescience.com/en/objectives/ucplfln/>.
- [33] “PLAPON Objectives.” *Olympus*.
[http://www.olympuslifescience.com/en/objectives/plapon/#!cms\[tab\]=%2Fobjectives%2Fplapon%2F60xo](http://www.olympuslifescience.com/en/objectives/plapon/#!cms[tab]=%2Fobjectives%2Fplapon%2F60xo).
- [34] B.O. Flynn and M.W. Davidson. “Coverslip Correction Collars.” *Nikon Microscopy U*. <https://www.microscopyu.com/tutorials/slipcorrection>.
- [35] “Immoil-F30CC Optics.” *Olympus*.
<http://www.olympus-lifescience.com/en/optics/immoil-f30cc/>.
- [36] “Large Beam Diameter Single-Axis Scanning Galvo Systems.” *Thorlabs*.
https://www.thorlabs.com/newgrouppage9.cfm?objectgroup_id=7616.
- [37] “Small Beam Diameter Scanning Galvo Mirror Systems.” *Thorlabs*.
https://www.thorlabs.com/newgrouppage9.cfm?objectgroup_id=3770&pn=GVS201#4419.
- [38] “How Laser Shows Work- Scanning Systems.” *LaserFX*.
<http://www.laserfx.com/Works/Works3S.html>.
- [39] “Galvo or Resonance Scanning Guide.” *Scientifica*.
<http://www.scientifica.uk.com/research-news/galvo-or-resonant-scanning-guide>.
- [40] S.L. Jacques, “Optical properties of biological tissue: a review.” *Physics in Medicine and Biology* **58**, (2013).

- [41] "PDMS: A Review." *Elve Flow*.
<http://www.elveflow.com/microfluidic-tutorials/microfluidic-reviews-and-tutorials/the-poly-di-methyl-siloxane-pdms-and-microfluidics/>.
- [42] "Spin Coating: A Guide to Theory and Techniques." *Ossila*.
www.ossila.com/pages/spin-coating.
- [43] R.B. Knowles, T. Gomez-Isla, and B.T. Hyman, "A β Associated Neuropil Changes: Correlation with Neuronal Loss and Dementia." *Journal of Neuropathology and Experimental Neurology* 57, 1122 (1998).